

Diptera vision and zebra stripes

KRISPIN M. DETTLAFF

krispind@ethz.ch

Department of Chemistry and Applied Biosciences

ETH Zürich

Vladimir-Prelog-Weg 2, CH-8093 Zürich, Switzerland

Abstract

The function of the zebra's striped coat has been debated since Darwin¹ and Wallace². A growing body of comparative^{3,4} and experimental evidence⁵⁻⁹ supports the hypothesis that the stripes act primarily as a defence against visually orienting biting Diptera — in particular tabanids (horse flies), glossinids (tsetse flies) and culicids (mosquitoes). The mechanisms proposed for this protection range from polarotactic disruption^{8,10} and silhouette break-up¹¹ to motion-based illusions arising in the Reichardt-type motion detectors of the insect visual system¹². In this work we focus on a complementary, purely optical mechanism: the Moiré interference that arises when a periodic striped stimulus is sampled by the periodic ommatidial lattice of an insect compound eye^{13,14}. We develop a linear, shift-invariant Fourier model of the diptera compound eye, parameterised from published optical data on diurnal Culicidae¹⁵⁻¹⁷, and apply it to images of zebra coats observed at biologically relevant viewing. The model predicts that, in a band of approach distances of approximately 1 m – 5 m, the interaction of the stripe pattern with ommatidial sampling generates parasitic spatial frequencies that are absent from the physical stimulus and that fall within the spatial-frequency window most relevant to host fixation and landing control¹⁸⁻²⁰. A post-retinal motion-detector stage demonstrates that these parasitic frequencies translate into spurious local motion vectors, consistent with the empirical observation that tabanid and glossinid flies fail to land cleanly on striped surfaces. Our results are therefore consistent with the biting-fly hypothesis of zebra striping.

Contents

1	Introduction	1
1.1	The riddle of the zebra’s stripes	1
1.2	Biting flies	1
1.3	Apposition compound eye	2
1.4	Moiré interference	2
2	Optical Model	3
2.1	Diptera vision	3
2.2	Distance scaling in Fourier space	4
2.3	Compound-eye transfer function	4
2.4	Apposition baseline	5
2.5	Sampling and reconstruction	5
2.6	Photoreceptor non-linearity	6
2.7	Moiré isolation	7
2.8	Quantifying parasitic content	7
3	Simulation	8
3.1	Image dataset and preprocessing	8
3.2	Compound-eye and ommatidial sampling	9
3.3	Numerical pipeline	10
3.4	Airy MTF	11
3.5	Regional variation in $\Delta\varphi$	12
3.6	Fourier model simulation	13
3.7	Post-retinal motion processing	15
3.8	Adaptive gain	16
3.9	Unstriped control	17
4	Discussion	17
4.1	Parasitic interference	18
4.2	Stripes vs. stripe-removed control	19
4.3	Regional variation	22
4.4	Chromatic channels	24
4.5	Polarisation channels	25
4.6	Landing failure on striped hosts	26
5	Conclusion	28
	Acknowledgements	28
	Supplementary Information	29
S.1	Gaussian approximation of the ommatidial acceptance	29
S.2	FFT-pipeline numerical controls	29
S.3	Photoreceptor non-linearity	29
S.4	Body-height calibration	30
S.5	Diagnostic for the Reichardt motion-energy control	31

1 Introduction

1.1 The riddle of the zebra's stripes

The black-and-white coat of plains, mountain and Grevy's zebras (*Equus quagga*, *E. zebra* and *E. grevyi*) is one of the most conspicuous coat patterns in the animal kingdom and has attracted scientific speculation for more than 150 years^{1,2,21–23}. At least five non-mutually-exclusive families of hypotheses have been formulated and reviewed in detail^{3,24,25}: crypsis or disruptive camouflage against large mammalian predators; predator confusion (“motion dazzle”)^{26–28}; intraspecific signalling, individual identification and group cohesion; thermoregulation through differential heating of the black and white stripes^{29,30}; and defence against haematophagous biting Diptera^{3,5,6,8}.

Phylogenetic and geographic evidence has progressively shifted the balance against the mammalian-predator hypothesis. Caro et al.³ mapped striping intensity on equid subspecies against the geographic distribution of putative selective agents and found a strong, repeated association of body, leg, belly and shadow striping with proxies for tabanid and tsetse activity, but no consistent association with predator distribution, woodland cover, group size or temperature maxima. Larison et al.⁴ reached partly different conclusions on plains-zebra populations using random-forest models, finding the strongest correlation with temperature; however the leg-stripe association resists a thermoregulatory explanation, and direct thermographic measurements indicate that stripes do not in fact lower the surface temperature of equid models exposed to solar radiation³⁰. The biting-fly hypothesis is the only one for which both comparative and direct experimental evidence co-exist^{5–9,11,31}.

1.2 Biting flies

Equids in tabanid- and glossinid-rich habitats can suffer severe blood loss, reduced grazing time and exposure to vector-borne pathogens including *Trypanosoma* spp.^{3,5}. The selective pressure exerted by chronic biting-fly attack is therefore non-trivial and, as Waage already argued, of an order comparable to predation pressure⁵. Diurnal biting Diptera locate their hosts through a multimodal sensory cascade. At long range, olfactory cues — CO₂, ammonia, short-chain fatty acids and species-specific kairomones — dominate^{32–34}. At intermediate range (a few metres), vision takes over: many tabanids exploit positive polarotaxis to detect dark, polarising surfaces such as wet skin or water, and use the same cue to home in on dark hosts^{8,10,11}. At close range, the landing manoeuvre itself is controlled by visual feedback from the optic flow expanding over the retina^{18–20}. A defensive coat pattern can therefore intervene at any of these stages: by reducing salience against the background¹¹, by depolarising reflected light^{8,10}, by interfering with the figure-ground segmentation that supports landing^{6,7}, or by injecting spurious motion signals into the optic-flow estimator¹².

1.3 Apposition compound eye

Diptera possess apposition compound eyes, in which each photoreceptor unit — the ommatidium — consists of a corneal lens, a crystalline cone and a fused or open rhabdom comprising eight reticular cells (R1–R8)^{15,16,35}. Two geometric quantities determine the spatial sampling of the visual scene: the lens facet diameter D (typically $15\ \mu\text{m} - 30\ \mu\text{m}$) and the inter-ommatidial angle $\Delta\varphi$ (typically $1^\circ - 5^\circ$)^{14,15}. Their product, the “eye parameter” $D\Delta\varphi$, has been used by Kawada et al.¹⁷ to classify culicid species along a continuum from diurnal (small eye parameter, higher resolution) to nocturnal (large eye parameter, higher photon catch). For *Aedes aegypti*, a diurnal anthropophilic vector used in this study as a representative of the Diptera $\Delta\varphi$ lies near 2.5° , corresponding to a Nyquist spatial frequency of about 0.2 cycles/deg^{15,16}.

Two consequences are central to the present work. First, the ommatidial array constitutes a regular, quasi-hexagonal sampling lattice. Like any regular sampler, it is liable to alias spatial frequencies above its Nyquist limit¹³. Second, the angular acceptance function of each rhabdom acts as a low-pass spatial filter^{13,36}. The combined optical transfer function (OTF) is therefore a low-pass envelope multiplied by a comb of resampling peaks¹⁴ — exactly the regime in which Moiré interference is generated.

1.4 Moiré interference

When two periodic structures with comparable spatial frequencies are multiplied — as occurs when a striped scene is sampled by the ommatidial array — the resulting signal contains not only the original spatial frequencies but also their sums and differences. Provided one of these difference frequencies falls within the eye’s pass-band, it appears in the retinal image as a low-frequency “parasitic” fringe pattern that has no physical counterpart on the zebra surface. This is the classical Moiré effect of optics and its impact on the diptera vision is studied in this publication.

The biological relevance of such an effect is demonstrated by its consistency with empirical observations. Zebra stripe widths span $\sim 0.2\ \text{cm} - 7.5\ \text{cm}$ across body regions and species⁸, which projects to spatial periods of $\sim 0.1^\circ - 4^\circ$ at viewing distances of $1\ \text{m} - 5\ \text{m}$, bracketing the ommatidial pitch of glossinids, culicids and tabanids. Tabanid attractiveness drops sharply for stripes narrower than the inter-ommatidial spacing⁸, with the empirical critical distance for *Glossina pallidipes* estimated at $\sim 3.5\ \text{m}$ for $20\ \text{cm}$ stripes⁶. Recent high-speed video of tabanids around live zebras and zebra-coated horses shows that flies approach at similar rates but fail to execute controlled landings, instead making aborted touchdowns or fly-bys⁹ behaviour consistent with corruption of the optic-flow signals that normally guide landing^{19,20}.

2 Optical Model

The following chapter describes how the diptera vision on Zebra can be modeled in a Fourier optic framework. It provides the theoretical basis for the following chapters.

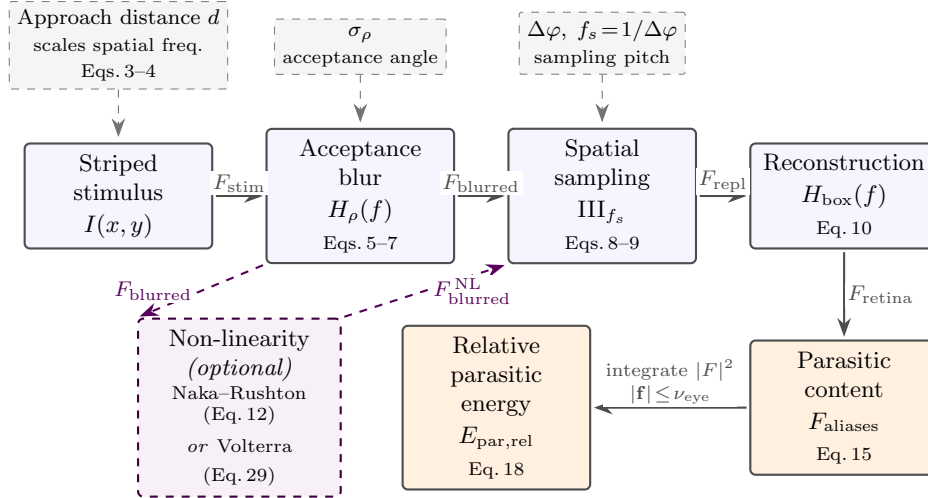


Figure 1: Optical-model scheme, the diptera eye is modelled as a cascade of four linear operations on the striped stimulus $I(x, y)$ (blue boxes): acceptance blur by the angular photoreceptor MTF H_ρ , spatial sampling by the Dirac comb III_{f_s} at the inter-ommatidial spacing $\Delta\varphi$, and Voronoi reconstruction by the box-cell aperture H_{box} . Three eye parameters control the chain (dashed boxes on top): the approach distance d scales the spatial-frequency content of the stimulus, the acceptance angle σ_ρ pins H_ρ , and the inter-ommatidial spacing $\Delta\varphi$ pins the comb pitch f_s . The output stages (orange boxes) extract the parasitic content F_{aliases} (Eq. 15) and integrate its power inside the eye Nyquist disc to obtain the dimensionless metric $E_{\text{par,rel}}$ (Eq. 18). An photoreceptor non-linearity (dashed violet branch) replaces F_{blurred} with $F_{\text{blurred}}^{\text{NL}}$ before sampling and produces a parallel parasitic signal $F_{\text{aliases}}^{\text{NL}}$ along the same final path.

2.1 Diptera vision

The spatial vision of the host-approaching diptera is modeled as a linear, shift-invariant optical system. A memoryless photoreceptor non-linearity is added as in §2.6. This idealization omits the temporally-adaptive gain control of the lamina and the post-receptor lateral interactions of the optic lobe^{14,18}, but it captures the essence of the phenomenon under study: the appearance of new spatial frequencies through the interaction of a periodic stimulus with a periodic sampling lattice^{13,15,16}.

The retinal image $I_{\text{retina}}(x, y)$ is the convolution of the external stimulus

$I_{\text{stim}}(x, y)$ with the spatial impulse response $h_{\text{eye}}(x, y)$ of the compound eye:

$$I_{\text{retina}}(x, y) = I_{\text{stim}}(x, y) * h_{\text{eye}}(x, y). \quad (1)$$

Spatial coordinates (x, y) are expressed in degrees of visual angle relative to the optical axis. The corresponding Fourier-domain relation is the product

$$F_{\text{retina}}(u, v) = F_{\text{stim}}(u, v) \cdot H_{\text{eye}}(u, v), \quad (2)$$

where (u, v) are spatial frequency coordinates in cycles deg^{-1} , $F_{\text{stim}} = \mathcal{F}\{I_{\text{stim}}\}$, and $H_{\text{eye}}(u, v)$ is the optical transfer function (OTF) of the compound eye.

The shift-invariance assumption is justified by the local and quasi-periodic structure of the ommatidial array. Across the few tens of degrees relevant for terminal host approach, the inter-ommatidial angle $\Delta\varphi$ varies by less than a factor of two, even between the acute zone and the rest of the eye^{15,16,35}, so the OTF can be approximated as locally constant.

2.2 Distance scaling in Fourier space

Viewing distance enters the model through the visual angle subtended by the host. Let $I_0(x, y)$ denote the stimulus expressed in degrees of visual angle at a reference distance d_0 , with the body height calibrated to a generic value. For a viewing distance d , the projected stimulus is uniformly rescaled,

$$I_{\text{stim}}^{(d)}(x, y) = I_0\left(\frac{d}{d_0}x, \frac{d}{d_0}y\right), \quad (3)$$

where the scale factor d/d_0 shrinks the angular extent of the animal. The Fourier scaling theorem gives

$$F_{\text{stim}}^{(d)}(u, v) = \left(\frac{d_0}{d}\right)^2 F_0\left(\frac{d_0}{d}u, \frac{d_0}{d}v\right), \quad (4)$$

i.e., as the diptera moves further from the host the stripe pattern shifts towards *higher* spatial frequencies in the angular spectrum. Distance therefore acts as a controlled spectral sweep that determines which components of the stripe pattern fall into resonance with the fixed sampling lattice of the eye.

2.3 Compound-eye transfer function

The dipteran-eye OTF is modelled as the product of two physically motivated factors: a low-pass envelope H_ρ representing the angular acceptance function of a single ommatidium^{13,14}, and a sampling factor H_{samp} that encodes the periodic ommatidial lattice^{15,16}:

$$H_{\text{eye}}(u, v) = H_\rho(u, v) \cdot H_{\text{samp}}(u, v). \quad (5)$$

Treating each ommatidium as a diffraction-limited optical system with a circular facet aperture of diameter D operating at wavelength λ , the angular point-spread function is the Airy pattern:

$$\text{PSF}(\theta) = \left[\frac{2 J_1(\pi D \theta / \lambda)}{\pi D \theta / \lambda} \right]^2, \quad (6)$$

where J_1 is the Bessel function of the first kind of order one and θ is the off-axis angle. The corresponding low-pass envelope H_ρ is obtained as the normalised autocorrelation of the circular pupil and is the standard diffraction-limited OTF for incoherent imaging^{37,38}:

$$H_\rho(u, v) = \begin{cases} \frac{2}{\pi} \left[\arccos\left(\frac{\rho}{\rho_c}\right) - \frac{\rho}{\rho_c} \sqrt{1 - \left(\frac{\rho}{\rho_c}\right)^2} \right], & \rho \leq \rho_c, \\ 0, & \rho > \rho_c, \end{cases} \quad (7)$$

with $\rho = \sqrt{u^2 + v^2}$ the radial spatial frequency and $\rho_c = D/\lambda$ the diffraction cutoff in cycles per radian. For diurnal culicids such as *Aedes aegypti* the interommatidial angle is $\Delta\varphi \approx 2^\circ$ ^{15,16}; matching the half-power width of Eq. (6) to the measured acceptance half-angle of $\sim 0.85^\circ$ yields $\rho_c \approx 34.7$ cycles/rad (≈ 0.61 cycles/ $^\circ$), which is adopted throughout this paper. The sampling factor H_{samp} is left abstract here; its exact form is the subject of §2.5.

2.4 Apposition baseline

In the apposition compound eye of *Aedes aegypti* each ommatidium possesses its own dioptric apparatus and a single, isolated rhabdom; the receptor signals are not pooled across neighbouring ommatidia in the lamina, in contrast to the neural superposition characteristic of higher Diptera (Calliphoridae, Drosophilidae) where seven coaligned receptors from seven neighbouring facets converge on one cartridge^{14,18,39}. Even in higher Diptera the convergence is a coherent summation of *coaligned* signals that increases sensitivity but preserves angular resolution. The implication for the present model is that the only physical neighbour coupling in the optical front-end is the partial overlap of the angular acceptance functions of adjacent ommatidia, which is already captured by H_ρ (Eq. 7; $\sigma_\rho = 0.85^\circ$, FWHM $\Delta\rho \approx 2^\circ$ for an inter-ommatidial angle $\Delta\varphi = 2.5^\circ$). After acceptance blur, each ommatidium acts as an independent point sampler.

2.5 Sampling and reconstruction

Ommatidial sampling on the lattice $\Lambda_{\Delta\varphi} = \{(m\Delta\varphi, n\Delta\varphi) \mid m, n \in \mathbb{Z}\}$ is, in the spatial domain, multiplication of the acceptance-blurred stimulus by a two-dimensional Dirac comb,

$$I_{\text{samples}}(x, y) = I_{\text{blurred}}(x, y) \cdot \text{III}_{\Delta\varphi}(x, y), \quad I_{\text{blurred}} = I_{\text{stim}} * h_\rho, \quad (8)$$

where $\text{III}_{\Delta\varphi}(x, y) = \sum_{m,n} \delta(x-m\Delta\varphi) \delta(y-n\Delta\varphi)$ and $h_\rho = \mathcal{F}^{-1}\{H_\rho\}$. The dual statement in the frequency domain is convolution of the blurred-stimulus spectrum with the dual comb at spacing $f_s = 1/\Delta\varphi$,

$$F_{\text{repl}}(u, v) = F_{\text{blurred}}(u, v) \circledast \text{III}_{f_s}(u, v) = \sum_{k,m} F_{\text{blurred}}(u - kf_s, v - mf_s), \quad (9)$$

where \circledast denotes two-dimensional convolution. The $(k, m) = (0, 0)$ term reproduces the signal the eye would deliver if sampling were ideal; every other (k, m) term is a spectral replica of F_{blurred} shifted by integer multiples of f_s along each axis. Spectral content of these replicas that falls inside the eye's Nyquist disc $|f| \leq \nu_{\text{eye}} = 1/(2\Delta\varphi)$ is the moiré signal: frequencies the brain receives but that the stimulus did not contain.

Each ommatidium represents an angular Voronoi cell (a $\Delta\varphi \times \Delta\varphi$ square for a square lattice). By using the – “nearest-neighbour” – reconstruction rule to every direction the value reported by the closest ommatidium is assigned, which spatially is convolution of the spike train with a square indicator function of side $\Delta\varphi$. The Fourier-domain twin is multiplication by the corresponding box transfer function,

$$H_{\text{box}}(u, v) = \text{sinc}(\Delta\varphi u) \text{sinc}(\Delta\varphi v), \quad (10)$$

with $\text{sinc}(x) = \sin(\pi x)/(\pi x)$. The full linear retinal spectrum is then

$$F_{\text{retina}}(u, v) = H_{\text{box}}(u, v) \sum_{k,m} F_{\text{blurred}}(u - kf_s, v - mf_s). \quad (11)$$

The sinc factors vanish exactly at $u, v = \pm kf_s$ for $k \geq 1$, so H_{box} kills replicas at the comb spike centres (the dark cross visible in the displayed spectra at $\pm f_s = \pm 0.40 \text{ cyc}/^\circ$). The sinc envelope decays as $1/u^2$ in each direction, so F_{retina} has finite total energy as required for a physically realisable image.

The inter-ommatidial angle $\Delta\varphi$ is taken from literature Land et al.¹⁵ and Kawada et al.¹⁷. A hexagonal-lattice variant is qualitatively unchanged in agreement with sampling theory¹³.

2.6 Photoreceptor non-linearity

The compressive response of insect photoreceptors is well described by a Naka–Rushton function^{14,40},

$$\text{NR}_{n,s_{50}}(s) = \frac{s^n}{s^n + s_{50}^n}, \quad (12)$$

with shape parameter $n = 0.7$ and half-saturation level $s_{50} = 0.5$. Inserted between the acceptance blur and the comb convolution, this point-wise non-linearity creates harmonic and intermodulation content $f_1 \pm f_2$, $2f_1$, $2f_1 \pm f_2$ that the strictly linear chain of §2.5 cannot generate. To make the contribution of this non-linearity explicit, a non-linear blurred image is defined

$$I_{\text{blurred}}^{\text{NL}}(x, y) = (1 - \alpha) I_{\text{blurred}}(x, y) + \alpha \text{NR}_{n,s_{50}}(I_{\text{blurred}}(x, y)), \quad (13)$$

with mix factor $\alpha \in [0, 1]$ interpolating between linear ($\alpha = 0$) and fully compressed ($\alpha = 1$). The remainder of the chain is unchanged but uses $F_{\text{blurred}}^{\text{NL}} = \mathcal{F}\{I_{\text{blurred}}^{\text{NL}}\}$ in place of F_{blurred} , giving

$$F_{\text{aliases}}^{\text{NL}}(u, v) = H_{\text{box}}(u, v) \sum_{k, m} F_{\text{blurred}}^{\text{NL}}(u - kf_s, v - mf_s) - F_{\text{blurred}}(u, v) H_{\text{box}}(u, v). \quad (14)$$

Subtracting the *linear* baseline $F_{\text{blurred}} \cdot H_{\text{box}}$ in Eq. 14 ensures that all content the brain receives but the stimulus optics alone do not supply – both sampling-induced replicas and harmonics created by the non-linearity itself – is counted as parasitic.

2.7 Moiré isolation

The signal the eye would have delivered with ideal sampling is $F_{\text{signal}} = F_{\text{blurred}} \cdot H_{\text{box}}$. Subtracting it from the full retinal spectrum (Eq. 11) leaves the parasitic content of every $(k, m) \neq (0, 0)$ replica multiplied by the same reconstruction MTF,

$$F_{\text{aliases}}(u, v) = F_{\text{retina}}(u, v) - F_{\text{blurred}}(u, v) H_{\text{box}}(u, v). \quad (15)$$

This is the definition of the parasitic spectrum used throughout this publication. By construction it is identically zero at every (u, v) where the brain receives the same content the acceptance-blurred stimulus already supplied; what survives are the genuinely added frequencies introduced by the sampling-and-reconstruction stage.

The spatial-domain image of the parasitic information is recovered by inverse Fourier transform,

$$I_{\text{par}}(x, y) = \mathcal{F}^{-1}\{F_{\text{aliases}}(u, v)\}, \quad (16)$$

yielding an angular map of the artificial contrast that arises exclusively from the interaction of the striped coat with ommatidial sampling. Every feature visible in I_{par} is a phantom percept — a spatial distribution of contrast with no physical counterpart on the host’s coat.

2.8 Quantifying parasitic content

The scalar that summarises a parasitic spectrum is its integrated power within the eye’s Nyquist disc:

$$E_{\text{par}}(d) = \sum_{|f| \leq \nu_{\text{eye}}} |F_{\text{aliases}}(u, v; d)|^2, \quad E_{\text{par}}^{\text{NL}}(d) = \sum_{|f| \leq \nu_{\text{eye}}} |F_{\text{aliases}}^{\text{NL}}(u, v; d)|^2. \quad (17)$$

By Parseval’s theorem these are equivalent to $\sum_{x, y} |I_{\text{par}}(x, y)|^2$ in the spatial domain. The restriction $|f| \leq \nu_{\text{eye}}$ is essential: parasitic content outside the Nyquist disc is invisible to the Diptera brain because the box reconstruction H_{box} has already filtered it out.

The raw E_{par} carries the units of $|F|^2$ summed over a frequency disc, i.e. (linear-intensity)² multiplied by an N -dependent FFT normalisation factor. It

is therefore only meaningful in comparisons where the input intensity scale and FFT gain are constant. To obtain a scale-invariant scalar that is intrinsic to the optics of the eye-plus-stimulus system and can be compared across images, cameras and runs, the *relative* parasitic energy

$$E_{\text{par,rel}}(d) = \frac{E_{\text{par}}(d)}{E_{\text{sig}}(d)}, \quad E_{\text{sig}}(d) = \sum_{|f| \leq \nu_{\text{eye}}} |F_{\text{blurred}}(u, v; d) H_{\text{box}}(u, v)|^2, \quad (18)$$

where E_{sig} is the integrated power of the alias-free in-band signal (the $k=m=0$ term of Eq. 11) – what the brain would receive if sampling were ideal at the same approach distance. The non-linear analogue uses the same denominator,

$$E_{\text{par,rel}}^{\text{NL}}(d) = E_{\text{par}}^{\text{NL}}(d) / E_{\text{sig}}(d). \quad (19)$$

Numerator and denominator are computed from the same FFT, on the same windowed image, over disjoint frequency supports, so the intensity, Hann-window and FFT-normalisation gains all cancel exactly in the ratio. $E_{\text{par,rel}}$ is therefore dimensionless and is the y-axis of every Fourier-stage parasitic-energy figure in this paper. The natural scale for $E_{\text{par,rel}}$ on photographs of striped hosts is the low-percent range. An idealised eye with a sampling lattice that resolves the stripe fundamental returns $E_{\text{par,rel}} \rightarrow 0$; the moiré mechanism is then absent. A diptera sampling lattice viewing the close-approach band $d \in [1, 2.5]$ m, by contrast, produces values that with $E_{\text{par,rel}} > 0$. This is the biologically relevant regime and will be discussed in §4.6. Because $E_{\text{par,rel}}$ is a ratio of squared-magnitude spectral sums it is non-negative by construction: at this Fourier stage the moiré can only add spectral power in the brain-accessible passband, never subtract from it. This non-negativity is a property of the optical stage alone. Downstream stages with a signed output (Hassenstein–Reichardt motion detector §3.7 do not inherit it, and a separate signed metric $E_{\text{HR}}^{\text{moiré}}$ (Eq. 26) is used for the corresponding Elementary Motion Detector (EMD) stage comparison in §4.6.

3 Simulation

This chapter describes how the optical model of §2 is realised numerically. Eq. 15 is the analytical target; the simulation reproduces every operation in that equation exactly in Fourier space, validates each FFT stage with a numerical control, and reports the relative parasitic energy of Eq. 18.

3.1 Image dataset and preprocessing

The pipeline is exercised on a set of photographs of *Equus quagga* (Nikon D50 with a 70–300 mm lens, typically $f = 300$ mm, $f/5.6$, ISO 400). The native angular pixel pitch is $\text{dpp}_{\text{cam}} = \arctan(p/f) \approx 5.42$ arcsec/pixel, derived from the XMP focal length f and a sensor pixel pitch $p = 7.88$ μm . Each image is converted to linear grayscale under the assumption of an sRGB gamma of 2.2.

A square region of interest centred on the body is selected on photograph; the resulting body height in camera pixels $h_{\text{body,pix}}$ together with the focal length determine the camera-to-host distance through

$$d_{\text{cam}} = \frac{h_{\text{body,m}}}{2 \tan(h_{\text{body,pix}} \cdot \text{dpp}_{\text{cam}}/2)}, \quad h_{\text{body,m}} = 1.4 \text{ m}. \quad (20)$$

The same chain is then evaluated at a sequence of diptera approach distances d by isotropic crop scaling: at each d the script extracts a square crop of side $(d/d_{\text{cam}}) \text{FoV}/\text{dpp}_{\text{cam}}$ camera-pixels around the chosen center, rescales it to the simulation grid $N=384$ samples per side, and feeds it to the chain of §2.1–§2.7. The body height is calibrated to a generic value $h_{\text{body}} = 1.4 \text{ m}$. As described above, the error thus included is reflected only in a shift to slightly higher or lower spatial frequencies in the angular spectrum and does not affect the absolute amount of parasitic energy.

3.2 Compound-eye and ommatidial sampling

The two geometric quantities that fully parameterise the sampling front-end of the model are the inter-ommatidial angle $\Delta\varphi$ and the angular acceptance half-width σ_ρ of a single ommatidium (Eq. 7–8). Both are empirically constrained in *Aedes aegypti* from goniometric and electrophysiological measurements^{14–16,35}. Figure 2 summarizes the geometry and the parameters adopted throughout the simulations. The left side sketches two adjacent ommatidia of the apposition compound eye, separated by the inter-ommatidial angle $\Delta\varphi = 2.5^\circ$, the diurnal-culicid value reported in Refs.^{15,16}. On the right side, the angular acceptance function $S(\theta)$ of one ommatidium is plotted. $S(\theta)$ is modelled as the diffraction-limited Airy pattern of a circular facet aperture (Eq. 6)^{13,37,38}, scaled so that its half-width at half maximum matches the empirical acceptance half-width $\sigma_\rho \approx 0.85^\circ$ – equivalently a full width at half maximum $\Delta\rho \approx 2^\circ$ – reported for diurnal Culicidae^{14–16}. The two curves correspond to two neighboring ommatidia i and $i+1$ whose optical axes are separated by $\Delta\varphi$. Their acceptance functions overlap only weakly at half-maximum, which determines the spatial-frequency cutoff of the eye through Eq. 7: the Airy MTF $H_\rho(u, v)$ has a hard diffraction cutoff at $\rho_c = D/\lambda$, with the aperture-to-wavelength ratio D/λ chosen so that the half-power width of the angular PSF matches the empirical acceptance half-width σ_ρ .

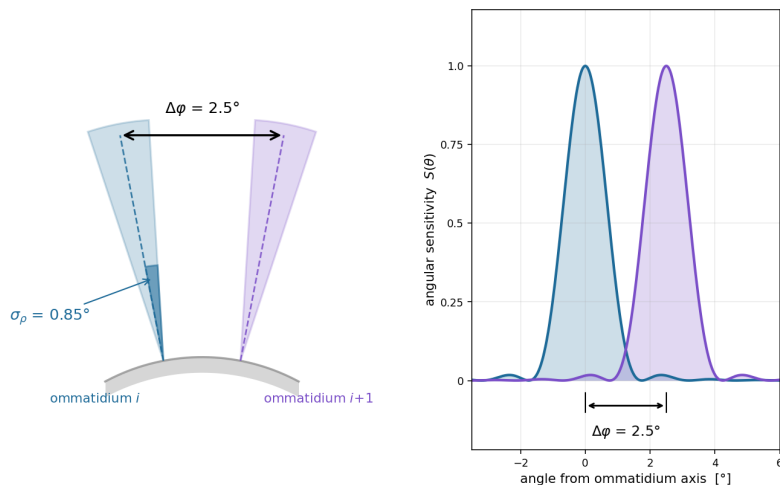


Figure 2: Compound-eye sampling geometry assumed in the simulation. The left side sketches two adjacent ommatidia of the apposition compound eye with inter-ommatidial angle and $\Delta\varphi$ and angular acceptance half-width σ_ρ . On the right side, the angular acceptance function $S(\theta)$ of one ommatidium is plotted.

For the simulations the standard *Aedes aegypti* parameter set $(\Delta\varphi, \sigma_\rho) = (2.5^\circ, 0.85^\circ)$ is adopted^{14–16}, which yields a sampling rate $f_s = 1/\Delta\varphi = 0.40 \text{ cyc deg}^{-1}$ and a corresponding Nyquist limit $\nu_{\text{eye}} = f_s/2 = 0.20 \text{ cyc deg}^{-1}$. Matching the half-power width of the Airy PSF (Eq. 6) to $\sigma_\rho = 0.85^\circ$ sets the aperture-to-wavelength ratio D/λ and therefore the diffraction cutoff of the Airy MTF (Eq. 7) at $\rho_c = D/\lambda \approx 0.61 \text{ cyc deg}^{-1}$, with a -3 dB amplitude point at $\rho \approx 0.23 \rho_c \approx 0.14 \text{ cyc deg}^{-1}$. The hard cutoff sits a factor of ~ 3 above ν_{eye} , so the spatial-frequency band $\nu_{\text{eye}} < \rho \leq \rho_c$ is a window of finite width that the optics transmits with non-zero MTF but the ommatidial sampling lattice cannot faithfully represent. This is precisely the regime in which the moiré mechanism of §2.7 operates: stripe fundamentals above the Nyquist limit but below the diffraction cutoff are not killed by the acceptance blur before they are aliased by the sampling comb. The same parameter set has been used by Warrant³⁶ as the canonical reference point for the apposition eyes of diurnal small-headed Diptera, is consistent with the comparative review of culicid eye optics by Kawada et al.¹⁷, and reproduces the antero-ventral acute-zone values reported in the recent vision survey of Hawkes et al.³⁵.

3.3 Numerical pipeline

$N = 384$ samples per side over a fixed angular canvas of $\text{FoV} = 30^\circ$ are used, yielding $\Delta x = \text{FoV}/N = 0.078^\circ$ per pixel. The FFT bin spacing is $\Delta f = 1/(N\Delta x) = 1/\text{FoV}$, and the comb shift in FFT-bin units is

$$\frac{f_s}{\Delta f} = \frac{N\Delta x}{\Delta\varphi} = \frac{\text{FoV}}{\Delta\varphi}. \quad (21)$$

For $\text{FoV} = 30^\circ$ and $\Delta\varphi = 2.5^\circ$ this is exactly 12, so the replica sum of Eq. 9 can be evaluated without sub-pixel interpolation by integer-shifted summation. When the canvas is fractionally off FoV (camera-pixel rounding produces 29.97° in practice), the comb shift becomes 11.99 bins; the corresponding sub-pixel spectral shift is implemented via the spatial-domain phase ramp $f_{\text{spatial}}(x, y) = \sum_{k, m} \exp(2\pi i (k f_s x + m f_s y))$, exact by Poisson duality. $|k|, |m| \leq 3$ replica shells (49 shifts in total) are summed up; higher-order shells contribute below floating-point noise inside the displayed window.

The simulated patch contains $(\text{FoV}/\Delta\varphi)^2 = 12 \times 12 = 144$ ommatidia, each separated by $\Delta\varphi = 2.5^\circ$. This is a focal sub-region of one eye, not the entire eye; a complete *Aedes aegypti* compound eye contains on the order of 350 ommatidia^{35,41} and covers a substantially larger solid angle. The choice $\text{FoV} = 30^\circ$ corresponds to the angular extent over which the assumption of a constant inter-ommatidial angle is reasonable in the antero-ventral acute zone^{15,16,35}; the regional variation away from this zone is treated explicitly in §3.5.

The simulation crop is not periodic. A rectangular FFT window introduces sinc-shaped leakage zeros that appear as a regular grid of dark pixels in the displayed power spectra, with no physical counterpart in the eye. A separable two-dimensional Hann window $w(x, y) = w_1(x) w_1(y)$ is applied to the spatial signals before each FFT, where w_1 is the standard one-dimensional Hann taper of length N . Because the same window factor multiplies F_{stim} , F_{blurred} and F_{retina} , the moiré-isolation difference of Eq. 15 is unaffected up to a constant gain. The Hann window is the only modification of the standard pipeline of §2.1 required by the Fourier-domain construction.

The Naka–Rushton compression of Eq. 13 is applied point-wise in the spatial domain on I_{blurred} , rescaled to zero-mean unit-variance before compression and re-matched to the original mean and variance after to remove global gain shifts. The compressed image is then re-Fourier-transformed and used as $F_{\text{blurred}}^{\text{NL}}$ throughout the non-linear branch (Eq. 14).

3.4 Airy MTF

The acceptance function H_ρ adopted throughout the main analysis (§2.3) is the diffraction-limited Airy pattern of an apposition lens of effective aperture D operating at wavelength λ ^{14,42}, with angular cutoff

$$f_c = D/\lambda \quad [\text{cyc}/\text{rad}]. \quad (22)$$

The closed-form circular-aperture MTF is

$$H_{\text{Airy}}(f) = \frac{2}{\pi} \left[\arccos(f/f_c) - (f/f_c) \sqrt{1 - (f/f_c)^2} \right] \quad \text{for } f \leq f_c, \quad (23)$$

zero above the cutoff. For *Aedes aegypti* facets $D \approx 15\text{--}25 \mu\text{m}$ operating around $\lambda \approx 500 \text{ nm}$, the diffraction cutoff sits at $\sim 2.4^\circ$ FWHM, comparable to the geometric acceptance angle $\Delta\rho \approx 2^\circ$ ¹⁵. Diffraction and rhabdom-aperture geometry therefore contribute roughly equally to H_ρ , and the Airy form captures both

the central lobe and the hard high-frequency cutoff that a Gaussian envelope (an approximation reviewed in §S.1) lacks. The simulation runs identically with either choice because the diffraction-limited MTF is a replaceable spatial filter, applied in the frequency domain. Replacing the Airy MTF with the Gaussian approximation of §S.1 ($D = 20 \mu\text{m}$, $\lambda = 500 \text{nm}$) leaves the moiré-peak distance unchanged but lowers the peak $E_{\text{par,rel}}$ by a factor of ~ 2 , because the Airy MTF has a sharper cutoff than the Gaussian envelope and therefore admits a larger fraction of the stripe-fundamental energy into the alias-generating band. The Gaussian approximation is in this sense a conservative under-estimate; the moiré-relevant approach distance and the existence of a clearly defined peak are PSF-invariant.

3.5 Regional variation in $\Delta\varphi$

The compound eye of *Aedes aegypti* is regionally specialised: the inter-ommatidial angle $\Delta\varphi$ varies across the visual field, with the antero-ventral region — the part that looks down and forward at a host during landing approach — having higher resolution than the dorsal periphery. Behavioural and anatomical work in Diptera links this acute zone specifically to host fixation and landing^{15,16}. The two ommatidia sketched in Fig. 2 represent the local geometry inside any one region; the regional difference between acute zone and periphery is a difference in the angle $\Delta\varphi$ between adjacent ommatidia (together with the corresponding acceptance half-width σ_ρ , which scales with the diameter of the rhabdom and is empirically smaller in the acute zone,^{14,15}).

A position-dependent $\Delta\varphi$ formally breaks shift-invariance: the OTF is no longer a single 2D filter, and a single global Fourier analysis cannot be applied. The numerical fix is piecewise-stationary regional analysis. Split the visual field into a small number of regions, run the existing pipeline independently in each region with its own $(\Delta\varphi, \sigma_\rho)$, and combine. The simulation supports this with three canonical configurations, with regional values estimated from the lens-diameter gradient documented in the references^{16,35} and propagated to the acceptance angle by the diffraction-limited optics of §2.3:

Foveal core	$\Delta\varphi = 1.5^\circ$, $\sigma_\rho = 0.6^\circ$
Standard (canonical acute zone)	$\Delta\varphi = 2.5^\circ$, $\sigma_\rho = 0.85^\circ$
Dorsal periphery	$\Delta\varphi = 3.5^\circ$, $\sigma_\rho = 1.2^\circ$

The Standard parameters reproduce the diurnal-culicid pair used throughout this study and represent a high-resolution diurnal culicid, comparable to the antero-ventral acute zone of *Aedes aegypti* or to *Toxorhynchites brevipalpis* (eye parameter $p \approx 1.1 \mu\text{m rad}$). Eye-averaged *Aedes aegypti* is substantially coarser ($\Delta\varphi \approx 6.40^\circ$, $p \approx 2.08 \mu\text{m rad}$ ⁴³), and applying the same pipeline at those parameters increases the peak $E_{\text{par,rel}}$ from $\sim 8\%$ to $> 40\%$ across the close-approach band. Within the family of biting Diptera the parasitic-energy fraction is therefore monotonic in $\Delta\varphi$ over the biologically relevant range: tabanids, glossinids and other culicid taxa with eye parameters between $p \approx 1$ and

$p \approx 3 \mu\text{m rad}$ would all show parasitic-energy fractions in the 8% to 40% range. The Standard parameter set is in this sense a conservative lower bound on the moiré effect; coarser-eyed biting flies see more parasitic content, not less.

The Foveal core row of the table is a model probe of a hypothetically more-resolved sub-region of the acute zone, and the Dorsal periphery row a corresponding probe in the opposite direction. The moiré mechanism is therefore not specific to culicids, and the quantitative shifts implied by family-level differences are captured by the same piecewise-stationary regional construction used here for within-eye variation. The biological interpretation of how the moiré signature varies across these regions is deferred to §4.3, where the resulting $E_{\text{par,rel}}(d)$ curves are reported (Fig. 7).

3.6 Fourier model simulation

A full pipeline output on a Zebra photograph (DSC_0085, *Equus quagga*) through the six stages of the cascade developed in §2.5–§2.7, ending at the non-linear parasitic image $\mathcal{F}^{-1}\{F_{\text{aliases}}^{\text{NL}}\}$ is shown in Fig. 3. Each column is one approach distance ($d \in \{0.5, 1.5, 2.5, 5\} \text{ m}$), each row one stage of the cascade. *Row 1 (Stimulus)*: angular cut-out at fixed FoV = 30° centred on the body; the camera-pixel side-length per column is given in the panel header. *Row 2 (Recovered blurred)*: inverse FFT of the windowed spectrum $F_{\text{blurred}} = \mathcal{F}\{I_{\text{blurred}} w\}$ after acceptance-MTF low-pass and Naka–Rushton compression — a numerical control on the FFT pipeline (round-trip relative error $\lesssim 10^{-15}$, §S.2). *Row 3 (Sampled image)*: inverse FFT of the comb-replicated spectrum $F_{\text{repl}} = F_{\text{blurred}} \otimes \text{III}_{f_s}$ (Eq. 9); each bright dot is one of the $(\text{FoV}/\Delta\varphi)^2 = 144$ ommatidial sample values. *Row 4 (Retinal image)*: inverse FFT of the reconstructed spectrum $F_{\text{retina}} = F_{\text{repl}} H_{\text{box}}$, i.e. the pixelated mosaic the post-sampling stages of the visual system actually receive. *Row 5 ($|F_{\text{aliases}}^{\text{NL}}|^2$)*: isolated parasitic power spectrum (Eq. 14); the white dashed circle marks the eye Nyquist limit $\nu_{\text{eye}} = 0.20 \text{ cyc deg}^{-1}$ and the dark cross-shaped band at $\pm f_s$ is the sinc-zero of the Voronoi reconstruction MTF. *Row 6 ($\mathcal{F}^{-1}\{F_{\text{aliases}}^{\text{NL}}\}$)*: the non-linear phantom percept on a symmetric red–blue scale; high-amplitude features systematically align with the black-to-white edges of the underlying coat (cf. §4.1).

Fig. 4 shows the relative parasitic energy $E_{\text{par,rel}}(d) = E_{\text{par}}(d)/E_{\text{sig}}(d)$ (Eq. 18) as function of the approach distance d ($\Delta d = 0.1 \text{ m}$), for the linear branch (blue circles, Eq. 15) and the non-linear Naka–Rushton branch (purple triangles, Eq. 14). The two curves agree closely, peak at the same approach distance and identify a moiré-relevant window $d \in [1, 2.5] \text{ m}$ (vertical dashed guidelines). The four distances marked in panel (a) anchor the four columns to their corresponding point on the energy curve. The qualitative reading of $E_{\text{par,rel}}(d)$ as function of the distance is subject of §4.1.

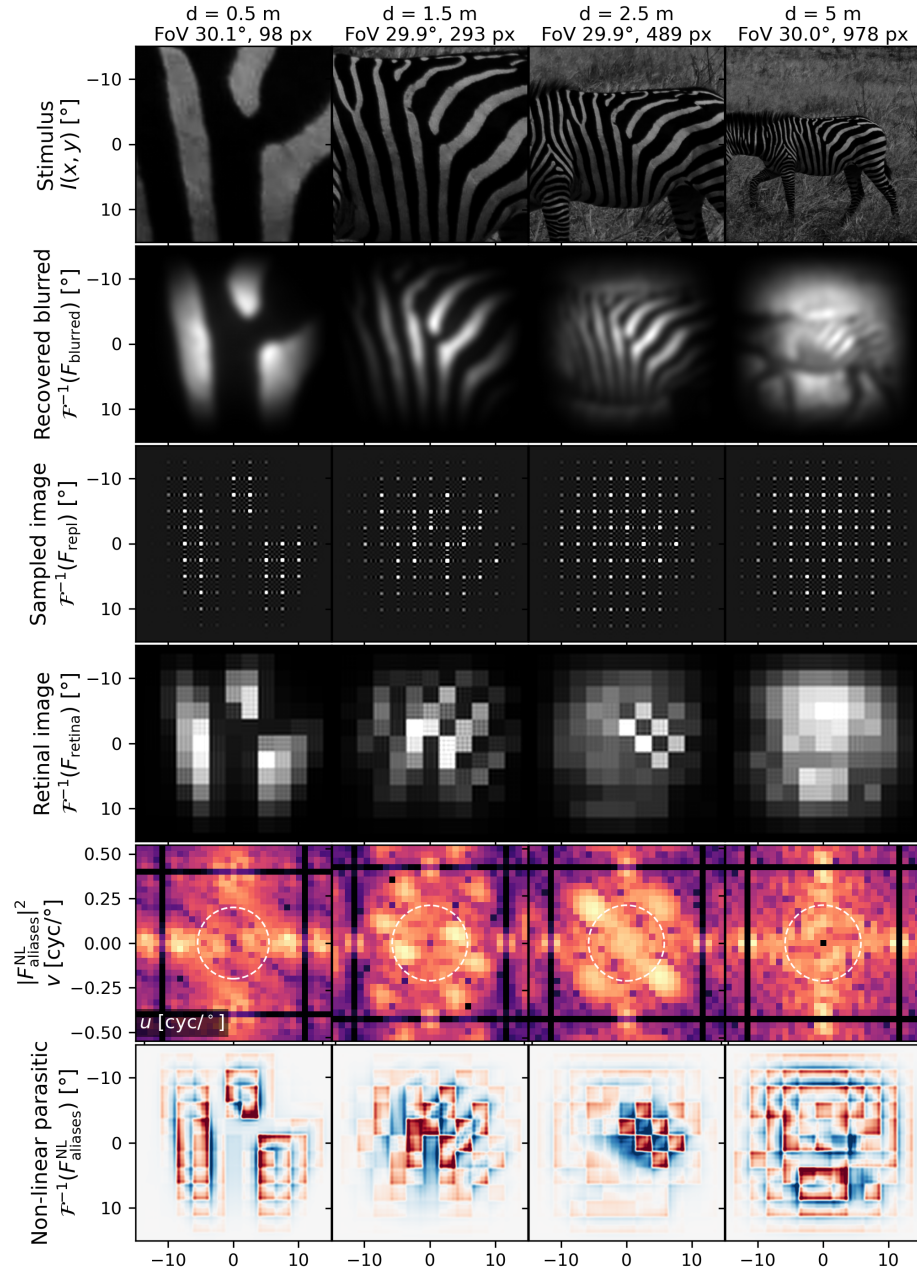


Figure 3: Full pipeline output on a single representative photograph (DSC_0085, *Equus quagga*). It tracks one approach distance per column ($d \in \{0.5, 1, 2.5, 5\}$ m) through the six stages of the cascade developed in §2.5–§2.7, ending at the non-linear parasitic image $\mathcal{F}^{-1}\{F_{\text{aliases}}^{\text{NL}}\}$.

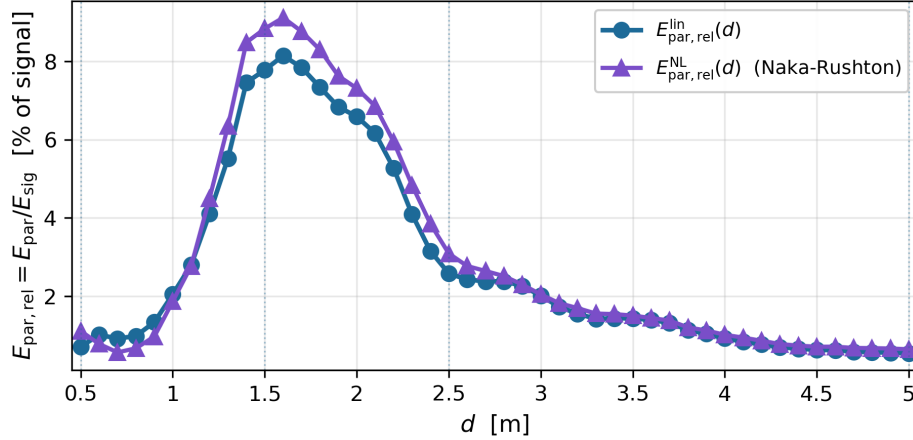


Figure 4: Reports the integrated relative parasitic energy $E_{\text{par,rel}}(d)$ (Eq. 18) as a function of approach distance, for both the linear (Eq. 15) and the non-linear branch (Eq. 14).

3.7 Post-retinal motion processing

To translate the parasitic retinal signal into a behaviourally meaningful prediction, a minimal model of the fly motion-detection pathway is fed with it. The Hassenstein–Reichardt elementary motion detector (EMD)^{44,45} correlates the temporally low-pass-filtered signal of one ommatidium with the un-filtered signal of an inter-ommatidial neighbour and subtracts the mirror-symmetric correlation. For two adjacent inputs $L(t)$ and $R(t)$ separated by $\Delta\varphi$,

$$\text{HR}(t) = [L(t) * \tau_{\text{p}}(t)] R(t) - L(t) [R(t) * \tau_{\text{p}}(t)], \quad (24)$$

where $\tau_{\text{p}}(t)$ is a first-order low-pass filter with time constant $\tau_{\text{HR}} \approx 30 \text{ ms}$ ^{18,45}. Eq. 24 is the opponent form of the detector: its output is a *signed* quantity per detector per frame, positive for motion in one direction along the $L \rightarrow R$ axis and negative for the mirror direction. The direction-agnostic motion energy at frame t is the squared output spatially averaged across the $N \times N$ detector array,

$$E_{\text{HR}}(t) = \langle \text{HR}_x(t)^2 \rangle + \langle \text{HR}_y(t)^2 \rangle, \quad (25)$$

with detectors applied independently in the horizontal and vertical directions and $N = 12$ ommatidia per side over the 30° simulated patch (one detector pair per neighbouring ommatidium).

A close-approach scenario of an attacking dipteran is simulated by re-cropping the photograph at successive equi-spaced approach distances $d(t) = d_0 - v_{\text{app}} t$ with $d_0 = 2.5 \text{ m}$, closing speed $v_{\text{app}} = 0.5 \text{ m s}^{-1}$, and frame interval $\Delta t = 30 \text{ ms}$, which delivers angular expansion rates inside the 20° s^{-1} to 200° s^{-1} range documented for in-flight tabanids⁹. Each frame of the approach trajectory is run twice through the optical pipeline of §3.3:

Full pipeline. Acceptance blur (H_ρ) \rightarrow Naka–Rushton ($\rightarrow I_{\text{blurred}}^{\text{NL}}$) \rightarrow comb-replication (Eq. 9) \rightarrow box reconstruction H_{box} . This delivers the actual ommatidial mosaic and therefore contains the aliased moiré of §2.7.

Clean pipeline. Identical to the full pipeline except that the comb-replication step is explicitly nulled ($F_{\text{aliases}}=0$ of Eq. 15). This is the same Naka–Rushton-compressed signal seen through the same box-reconstruction MTF, but without the spectral replicas that produce the moiré. It is the alias-free baseline against which the full pipeline is compared.

Because the two pipelines differ only in the comb step, subtracting their motion energies isolates the EMD-stage contribution of that step alone,

$$E_{\text{HR}}^{\text{moiré}}(t) = E_{\text{HR}}^{\text{full}}(t) - E_{\text{HR}}^{\text{clean}}(t). \quad (26)$$

Two properties of Eq. 26 are essential for reading the empirical results of §4.6 correctly. First, $E_{\text{HR}}^{\text{moiré}}$ is the difference of two mean-squared signed EMD outputs, not the squared magnitude of their difference, and therefore takes either sign: the comb step can either constructively augment or destructively cancel the genuine-motion EMD output before the per-detector squaring of Eq. 25. Second, this is categorically distinct from the Fourier-stage power ratio $E_{\text{par,rel}}$ of Eq. 18, which is non-negative by construction (a strict spectral addition). A moiré contribution that is a power addition at the optical stage can still subtract from the coherent motion percept at the EMD stage; the exact algebraic decomposition that isolates the cancelling (cross) and additive (self) components of $E_{\text{HR}}^{\text{moiré}}$ is reported in §5.5.

This motion-detection stage omits spatially-extended processing of the lobula plate and the gain control of the wide-field cells¹⁸, but is sufficient to test whether the parasitic spatial frequencies of §2 translate into measurable contamination of the local optic-flow signal that controls approach and landing in dipterans^{19,20}.

3.8 Adaptive gain

The receptor model used throughout this paper is the static Naka–Rushton compression of §2.6. This captures the steady-state saturation of insect photoreceptor response to light intensity, the property that does the substantive work in the Fourier pipeline of §2^{40,46,47}. Real receptors additionally have a slow membrane time constant $\tau_m \approx 10$ ms and a still-slower adaptation pool with characteristic time ~ 100 ms that drifts the operating point s_{50} toward the local mean luminance over time^{18,45,48}; the instantaneous gain is therefore set by recent stimulus history rather than by instantaneous luminance alone. However, the static formulation is the right choice for the research question of this paper, for two reasons that act in different parts of the pipeline.

For the Fourier-stage matched-pair analysis of §4.2 the choice is immaterial. The source images are photographic stills at a single fixed distance, the receptor is at its steady-state operating point in each frame, and an adaptive

cascade would collapse to the static Naka–Rushton compression already in use; light/dark history is irrelevant to the moiré-peak position and amplitude. The headline $E_{\text{par,rel}} \approx 8\%$ across the $n=28$ matched-pair dataset is invariant under this modelling choice.

For the Reichardt motion-energy control of §4.6 the choice is principled. That control presents each ommatidium with a true temporal sequence of luminances over a 4-second approach trajectory, with stripes translating across the visual field at angular speeds of 20–200 ° s⁻¹⁹, so adaptive dynamics would in principle modulate the per-frame contrast feeding Eq. 24. The static Naka–Rushton is retained because the purpose of the control is to isolate the EMD-stage consequence of the comb step (Eq. 9) on its own: a temporally varying gain acting on top of the comb would convolve two effects rather than expose one. The motion-energy values reported in Fig. 9 are therefore the static-receptor floor of the moiré-interference effect. The destructive-interference signature is also expected to survive under physiologically more realistic receptor dynamics: at the angular speeds above each receptor sees luminance transitions in the few-hundred-Hz range, well above the corner frequency of the adaptation low-pass (~ 10 Hz), and the adaptive gain therefore re-weights the slow body-silhouette envelope much more than the fast comb-step contribution. The substantive claim of §4.6 — that the comb step injects a strictly negative motion-energy contribution into the optic-flow estimate during close approach — does not depend on the receptor’s adaptive dynamics.

3.9 Unstriped control

The same construction applied to a uniformly coloured stimulus ($I_{\text{stim}} \equiv c$, or a plain grey Zebra) yields F_{stim} confined to a small low-frequency cluster around DC. The acceptance blur H_ρ leaves only DC content, so F_{repl} is a sparse comb at integer multiples of f_s , all of which are killed by the box reconstruction H_{box} (Eq. 10). Consequently $F_{\text{aliases}} \approx 0$ everywhere outside numerical noise, and $I_{\text{par}} \approx 0$. The vanishing of $\|I_{\text{par}}\|_2$ on uniform stimuli is a sanity check required by the sampling theorem¹³ and is exploited in the matched-pair test of §4.

4 Discussion

The simulation pipeline of §3 delivers, at every approach distance, two complementary outputs: the spatial parasitic image $I_{\text{par}}(x, y)$ and the dimensionless relative parasitic energy $E_{\text{par,rel}}(d)$ (Eq. 18). The discussion that follows interprets these outputs in four steps: (i) the matched-pair test that isolates the stripe pattern as the causal variable (§4.2); (ii) the distance dependence of the parasitic energy across a set of photographs, which identifies a peak at $d \in [1, 2.5]$ m that overlaps the documented terminal-hesitation window in which biting Diptera approach but fail to settle on striped hosts (§4.2); (iii) the robustness of the mechanism to two biologically important refinements — regional acute-zone specialisation and chromatic decomposition — followed by

the long-standing polarisation channel (§4.3–§4.5); and (iv) the propagation of this optical finding through a minimal Hassenstein–Reichardt motion-detector model (§4.6).

4.1 Parasitic interference

Figure 3 of §3.6 shows that the spatial parasitic image $\mathcal{F}^{-1}\{F_{\text{aliases}}^{\text{NL}}\}$ reproduces the geometry of the underlying retinal mosaic remarkably closely. In every column the high-amplitude red–blue features of the parasitic image lie precisely along the black-to-white boundaries of the striped stimulus rather than on the smooth interiors of either the dark or the bright stripes. This is a consequence of how sampling-induced moiré is generated: a stripe edge contains a broad range of spatial frequencies (the FFT of a step is $\propto 1/u$), so the edge populates the band $\nu_{\text{eye}} < |f| < 2\nu_{\text{eye}}$ much more strongly than the smooth stripe interior does. Replicas of that edge energy, shifted by $\pm f_s$ (Eq. 9), fold back into the eye’s Nyquist disc and appear in F_{aliases} as the dominant contribution to the parasitic content. In the spatial domain this manifests as the alternating red–blue ripple localised around every black-to-white edge of the zebra coat visible in row 6 of Fig. 3. The colour scale of row 6 encodes the sign of $\mathcal{F}^{-1}\{F_{\text{aliases}}^{\text{NL}}\}$ on a diverging red–blue scale (red positive, blue negative) and is normalised independently in each column to the 99th percentile of $|I_{\text{par}}|$, so colour saturation is comparable across columns only in terms of relative within-column spatial structure; the absolute amount of parasitic energy at each distance is quantified in Fig. 4 ($E_{\text{par,rel}}$), not by the colour intensity of row 6. The plausibility of this reading is reinforced by the distance dependence: at $d=0.5$ m the FoV captures essentially one large stripe transition and the parasitic image is correspondingly sparse; at $d=1.5$ m, where many stripes are present and edge density is highest, the parasitic image is densest; at $d=5$ m, where the stripes are angularly small but still resolvable, the edge density is lower again. The proximate predictor of moiré energy is therefore not edge density on the body nor fractional stripe area, but the angular edge density on the retina at the viewing distance d .

The dimensionless metric $E_{\text{par,rel}}(d)$ (Eq. 18) plotted in Fig. 4 quantifies this geometric resonance. The curve has a clear peak in the close-approach range $d \in [1, 2.5]$ m and falls off rapidly outside it. The peak location is set by an interplay between two competing effects. At small d the body subtends a large angular size and few stripes fit within the simulated FoV — many of the stripe transitions sit outside the analysed patch, so their contribution to the alias energy is missing. At large d the stripe pattern shrinks angularly until its dominant frequencies exceed the eye’s Nyquist limit; the acceptance-angle MTF (Eq. 7) attenuates them before they can be sampled, leaving little to alias. Between these limits there is a window in which several full stripe periods fit in the FoV and the dominant stripe frequency lies within or just above the eye Nyquist limit, so that f_s -shifted replicas fold back into the eye’s pass-band. For the canonical *Aedes aegypti* parameter set ($\Delta\varphi = 2.5^\circ$, $\sigma_\rho = 0.85^\circ$, $f_s = 0.40$ cyc deg⁻¹) and a body height ~ 1.4 m, this window centres on $d \approx 1.5$ m — well inside the close-approach range relevant for terminal landing^{5–7,9}.

The linear branch $E_{\text{par,rel}}^{\text{lin}}$ (Eq. 15) and the Naka–Rushton branch $E_{\text{par,rel}}^{\text{NL}}$ (Eq. 14) agree to within a few percent at the peak. The dominant contribution to the parasitic content is therefore geometric moiré — sampling-induced aliasing — rather than harmonic distortion injected by the photoreceptor non-linearity. The Naka–Rushton compression adds a measurable but subordinate amount of in-band intermodulation^{14,40}; the closed-form linear construction of Eq. 15 is consequently an adequate analytical handle on the mechanism.

4.2 Stripes vs. stripe-removed control

The most direct empirical test of the moiré hypothesis isolates the role of the stripe pattern itself by removing it from the host while leaving everything else — silhouette, body size, framing, lighting, background — byte-for-byte identical. Following the unstriped-control argument of §3.9, such a test has been constructed by digitally re-rendering each striped photograph with the stripes painted out to a uniform grey of matched local luminance, producing a stripe-removed twin, referred as horse condition. The same Fourier-moiré pipeline (§3.3) is run independently on both members of every pair, with the picker centre and body height set once on the striped image and transferred 1:1 to the no-stripes image; the script enforces equal pixel resolution and equal focal length, so this transfer requires no scaling.

Figure 5 shows the result of this matched-pair test. Stage-by-stage construction on two representative pair (zebra DSC_0084, DSC.0084 and their stripe-removed twin) at $d \approx 1.5$ m, FoV = 29.9°, 315 camera pixels per side. The seven rows trace the same cascade as Fig. 3 side by side for the two conditions: input photograph, stimulus crop, recovered blurred image, sampled image, retinal mosaic, parasitic power spectrum $|F_{\text{aliases}}^{\text{NL}}|^2$ (dashed circle marks $\nu_{\text{eye}} = 0.20$ cyc deg⁻¹), and parasitic image $\mathcal{F}^{-1}\{F_{\text{aliases}}^{\text{NL}}\}$. The striped zebra (left column) generates a structured parasitic spectrum $|F_{\text{aliases}}^{\text{NL}}|^2$ that concentrates inside the eye Nyquist disc, and an inverse-transform parasitic image that traces the body-aligned moiré fringes discussed in §4.1. The stripe-removed control (right column) is run through the identical pipeline; its parasitic spectrum and inverse transform contain no body-aligned structure, only the silhouette-edge ringing that any bounded image must generate when sampled on a discrete grid. The qualitative reading is that the parasitic content of the zebra column is genuinely caused by the stripe pattern, not by any other property of the scene (silhouette, mean luminance, framing, lighting), and the visual difference between the corresponding columns makes this immediate.

Figure 6 quantifies the same statement across $n = 28$ matched zebra/no-stripes pairs. Each pair consists of a striped zebra photograph (Nikon D50, $f = 300$ mm, $f/5.6$, ISO 400) and a digitally re-rendered twin in which the stripes are painted out to a uniform grey of matched local luminance, with silhouette, body size, framing, lighting and background preserved exactly. The Fourier-moiré pipeline of §3.3 is run independently on every member of every pair, with diffraction-limited Airy MTF (Eq. 23, $D = 20$ μm , $\lambda = 500$ nm) and Naka–Rushton receptor non-linearity (Eq. 12, mix $\alpha = 0.5$). The cross-pair

mean $\langle E_{\text{par,rel}}^{\text{NL}}(d) \rangle$ (solid markers, $\Delta d = 0.1\text{m}$) of the striped condition show the characteristic broad peak centred on $d \approx 1.4\text{m}$ with mean amplitude of order 10 % of the in-band signal, whereas the corresponding curves for the no-stripes condition (open markers) remain at the floor below $\sim 1\%$ across the full sweep. The peak ratio between the two conditions is approximately 10–20 \times inside the moiré-relevant band $d \in [1, 2.5]\text{m}$. Because $E_{\text{par,rel}}$ is by construction gauge-invariant — the per-image gain factors (intensity normalisation, FFT normalisation, Hann-window gain) cancel exactly between numerator and denominator (§2.8) — the stripes-vs-no-stripes gap of Fig. 6 cannot be attributed to per-image differences in exposure, brightness or framing. It is a gauge-invariant statement about the optics of the eye-plus-coat system. The thin background traces in the same panel show the per-pair curves. Every single pair in the dataset reproduces the same gap, with peak distances scattered slightly around 1.6 m in a manner consistent with different intrinsic angular stripe periods (finer-striped individuals shift the peak toward smaller d , in agreement with Eq. 4 and with the edge-density argument of §4.1). A further small source of horizontal scatter on the same peak is the calibration uncertainty in the assumed body height $h_{\text{body}} = 1.4\text{m}$. An inter-individual range of $1.35\text{m} \leq h_{\text{body}} \leq 1.45\text{m}$ propagates linearly through the angular projection to a $\pm 6\text{cm}$ shift in d_{peak} at $d_{\text{peak}} \approx 1.6\text{m}$, well below the natural width of the peak. Further information is given in §S.4. The observation that $E_{\text{par,rel}}$ collapses by more than an order of magnitude when the stripes alone are removed from a real photograph is direct empirical evidence that the moiré content predicted by the optical model (§2.7) is genuinely caused by the interaction of the stripe pattern with the ommatidial sampling lattice. The moiré peak is robust to model details, because the mechanism is dominated by geometric sampling-induced aliasing rather than by photoreceptor harmonic distortion. Quantitatively, $\sim 10\%$ of the energy the brain receives inside its own Nyquist disc, at the distance at which a tabanid or culicid would commit to landing, is genuinely parasitic moiré content with no physical counterpart on the coat. This is a non-trivial fraction of the available signal and is exactly the band in which the optic-flow estimator that controls the final landing manoeuvre operates^{18–20}. The moiré-relevant distance band identified by Fig. 6, $d \in [1, 2.5]\text{m}$, overlaps exactly with the documented terminal-hesitation phase during which biting Diptera approach a striped host but fail to settle^{5–7,9}. Beyond $\sim 3\text{m}$ the stripes-vs-no-stripes gap collapses because the body shrinks below the eye’s sampling resolution and the residual alias content is dominated by the silhouette edge itself rather than by any internal pattern. At these larger distances host-finding is in any case dominated by olfactory cues^{32–34}.

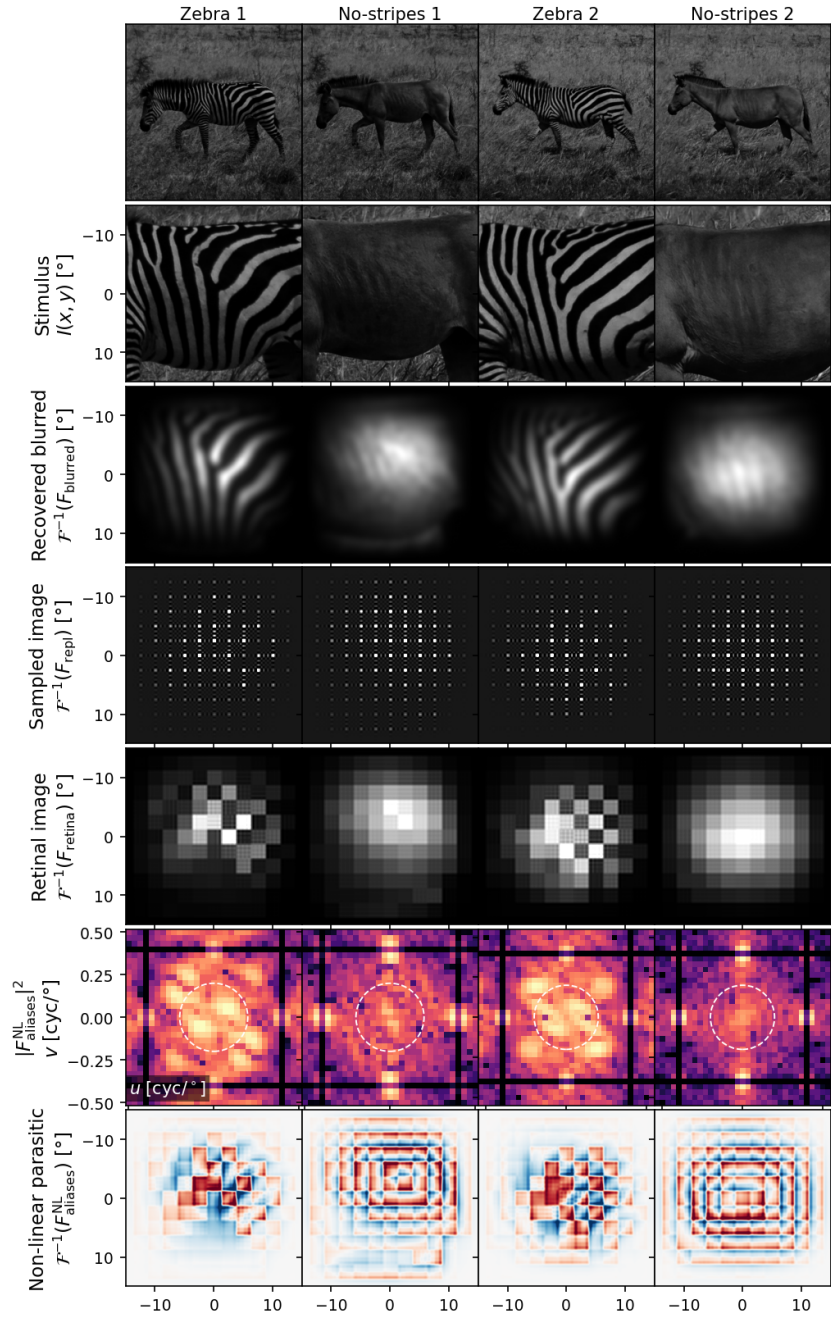


Figure 5: Full pipeline output on two matched pair (zebra, left column; stripe-removed control, right column). It tracks through the six stages of the cascade developed in §2.5–§2.7, ending at the non-linear parasitic image $\mathcal{F}^{-1}\{F_{\text{aliases}}^{\text{NL}}\}$.

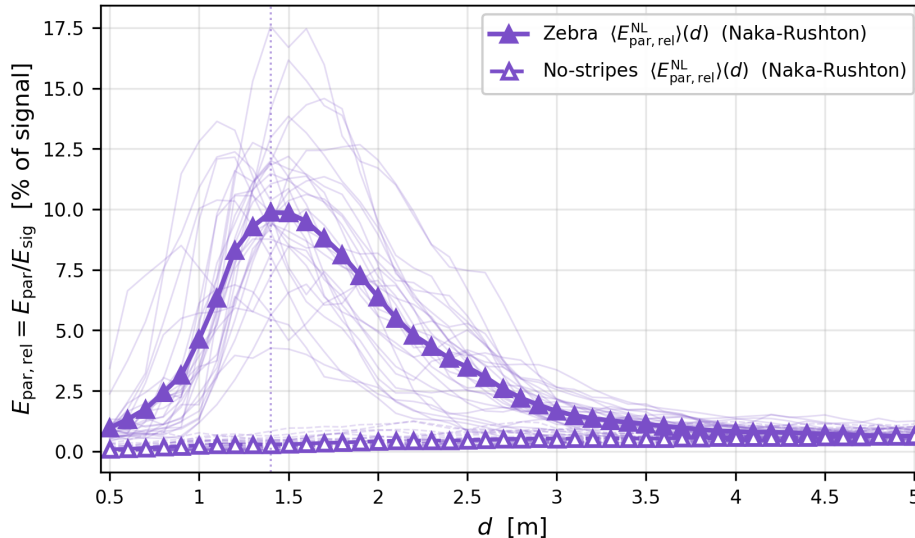


Figure 6: Integrated relative parasitic energy $E_{\text{par,rel}}(d)$ (Eq. 18) of matched pair (zebra, stripe-removed control) as a function of approach distance. Thin background traces: per-pair curves. Solid markers and solid means: stripes (zebra) condition; open markers and open means: stripe-removed control. The vertical dashed guideline marks the cross-pair mean moiré-peak distance $d \approx 1.4$ m.

4.3 Regional variation

The simulations of §3.6 use the Standard (canonical acute zone) parameter set $(\Delta\varphi, \sigma_\rho) = (2.5^\circ, 0.85^\circ)$, the diurnal-culicid value reported in the comparative-visual literature^{14–16}. The compound eye is, however, regionally specialised: the inter-ommatidial angle $\Delta\varphi$ varies systematically across the visual field, with the antero-ventral region — the part that looks down and forward at a host during landing approach — having higher resolution than the dorsal periphery^{15,35}. To probe how robust the moiré mechanism is to this regional specialisation, the piecewise-stationary construction of §3.5 is run independently in each of the three canonical configurations: *Foveal core* ($\Delta\varphi = 1.5^\circ$, $\sigma_\rho = 0.6^\circ$), *Standard* (2.5° , 0.85°), and *Dorsal periphery* (3.5° , 1.2°).

Figure 7 shows $E_{\text{par,rel}}^{\text{NL}}(d)$ for the three regions on a representative zebra photograph (DSC_0085). All three regions exhibit a clearly defined moiré peak with a comparable shape, but the peak distance and peak magnitude both shift systematically with $\Delta\varphi$. The dorsal periphery ($\Delta\varphi = 3.5^\circ$, purple) reaches its maximum at the smallest distance ($d \approx 0.9$ m, purple vertical dashed line) with the largest peak amplitude ($\sim 31\%$ of signal); the Standard configuration ($\Delta\varphi = 2.5^\circ$, blue) peaks at intermediate distance ($d \approx 1.1$ m) with intermediate amplitude ($\sim 14\%$); and the Foveal core ($\Delta\varphi = 1.5^\circ$, red) peaks at the largest distance ($d \approx 2.2$ m, red vertical dashed line) with the smallest peak amplitude

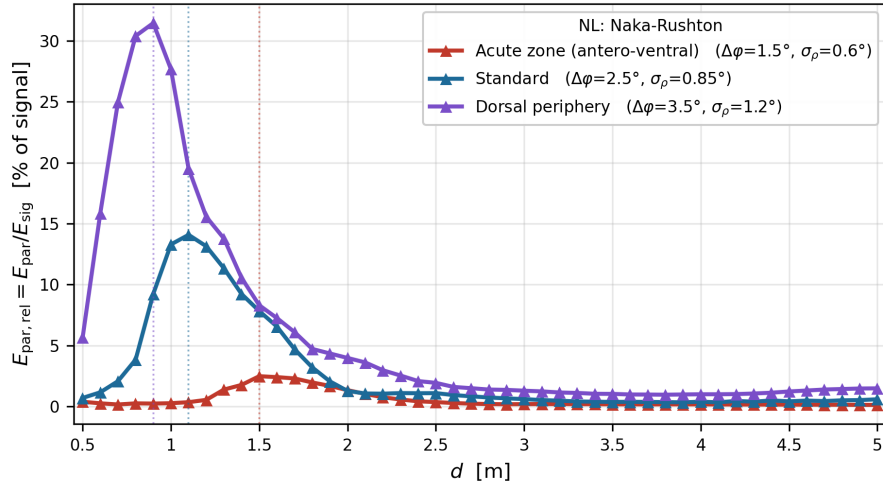


Figure 7: Regional sweep across the three canonical eye configurations of §3.5 on photograph DSC_0158. Foveal core (red), Standard / canonical acute zone (blue), Dorsal periphery (purple).

($\sim 2.5\%$). The ordering follows directly from the moiré-resonance condition between stripe period and sampling period: a finer sampling lattice has its Nyquist limit at a higher angular spatial frequency, so the alias-generating band is reached only when the stripes themselves shrink angularly — i.e. at larger approach distance — and the resonance lobe is correspondingly weaker because fewer stripe edges sit close to the Nyquist limit at that distance.

Two points stand out. First, the Foveal core still produces a clearly identifiable moiré peak: the mechanism does not disappear when the inter-ommatidial angle is reduced by 40% relative to the Standard parameter set. Second, the Foveal-core peak sits at $d \approx 1.5$ m, which is deeper into the close-approach band than the Standard or Dorsal-periphery peaks. Anatomically and behaviourally, the antero-ventral acute zone — of which the Foveal core is the highest-resolution sub-region — is the part of the eye specialised for host fixation and the terminal landing manoeuvre^{15,16,35}; it is the region whose output is read out by the descending neurons that drive the legs-out, hover, settle sequence^{18–20}. Placing the moiré peak of the most-resolved sub-region at the exact distance at which a tabanid or culicid has committed to landing ($\sim 1–2$ m) is therefore not a weakening of the mechanism but a strengthening of its biological relevance: the parasitic content is injected into the part of the visual pathway that drives the behaviour the field studies report disrupted^{5,7,9}.

The Dorsal-periphery peak, conversely, sits at $d \approx 1.0$ m. The dorsal eye is not the part of the visual field used for landing; it serves orientation and obstacle avoidance^{14,15}. A larger moiré peak in this region is therefore less behaviourally costly, although a fly performing close-range orientation manoeuvres around a

host body may still receive phantom-motion input from the dorsal mosaic. The moiré mechanism is robust to regional variation in $\Delta\varphi$, and is strongest where it matters most.

4.4 Chromatic channels

The simulation runs on a single-channel grayscale stimulus, which is appropriate for a first-principles demonstration of the geometric moiré mechanism but ignores the chromatic structure of the input. *Aedes aegypti* expresses at least three opsins with peak spectral sensitivities in the UV (~ 350 nm), blue (~ 425 nm), and green (~ 525 nm) bands^{49,50}; behavioural work confirms host attraction to multiple wavelengths³⁴. A chromatically faithful Fourier model compute the spectral irradiance of the stimulus at each opsin sensitivity and run the existing pipeline in parallel on each channel⁵¹. The simulation framework supports a per-channel sweep (RGB).

Figure 8 shows $E_{\text{par,rel}}^{\text{NL}}(d)$ for the three camera RGB channels of one representative zebra photograph (DSC_0084), each run through the pipeline with a diffraction-limited Airy MTF tuned to the centre wavelength of the channel ($\lambda_R = 620$ nm, $\lambda_G = 540$ nm, $\lambda_B = 460$ nm). The three curves share the same qualitative shape — a single clear peak in the close-approach band — but differ in peak amplitude. The blue channel ($\lambda_B = 460$ nm) produces the largest moiré response, peaking near $d \approx 1.1$ m with $E_{\text{par,rel}}^{\text{NL}} \approx 13.1\%$. The green channel ($\lambda_G = 540$ nm) peaks at the same position ($d \approx 1.1$ m) with intermediate amplitude ($\sim 10.8\%$), and the red channel ($\lambda_R = 620$ nm) is the weakest of the three ($\sim 8.1\%$) and peaks slightly earlier at $d \approx 1.0$ m. The peak *distance* is essentially channel-invariant; the peak *magnitude* scales inversely with the wavelength of the Airy MTF.

The Airy diffraction cutoff (Eq. 22) is larger at shorter wavelengths, so the blue channel admits a larger fraction of the stripe-fundamental energy into the alias-generating band before the diffraction MTF attenuates it. Further, zebra coats are known empirically to exhibit higher visible contrast in the blue and UV bands than in the red^{3,10}: spectroradiometric characterisation of plains zebra (*Equus quagga*) coat reflectance shows that white stripes return more UV/blue light relative to dark stripes than red light, so the per-channel modulation amplitude entering the FFT is higher at the blue end of the spectrum.

The photoreceptors most exposed to the moiré effect during close approach are the short-wavelength opsins. In *Aedes aegypti* these are the R7 UV-sensitive photoreceptors and the blue-sensitive R8 photoreceptors, both of which are known to play a dominant role in host fixation and dark target detection^{34,49,50}. The moiré mechanism therefore preferentially corrupts the chromatic channel that the diptera itself relies on most heavily for close-range host fixation. The peak *distance* is unchanged across channels because the moiré-resonance condition is *geometric* rather than *chromatic*; the chromatic channels modulate the peak amplitude through a combination of diffraction MTF and per-channel coat contrast, but not the distance at which the peak occurs.

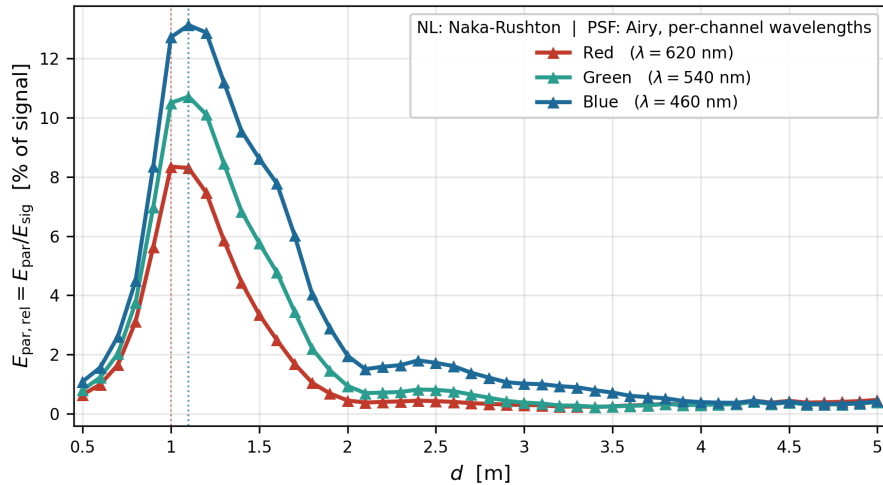


Figure 8: Chromatic-channel sweep across the three camera RGB channels of photograph DSC_0084 with per-channel Airy MTF.

4.5 Polarisation channels

Aedes aegypti ommatidia contain two orthogonal sets of microvilli within each rhabdomere, conferring polarisation sensitivity on the photoreceptors⁵². The behavioural relevance of polarisation cues for host-seeking biting flies is well established: dark, flat surfaces reflect strongly horizontally-polarised light, and tabanids and culicids exploit this signature for long-range detection of water and dark hosts^{8,10}. Crucially, white zebra stripes depolarise the reflected light, so the polarisation pattern of a striped coat does not match the “flat-dark-surface” template, and long-range polarotactic attraction to a zebra is reduced^{8,10,31}.

In a Fourier-optics framework, polarisation can be incorporated as three parallel chains operating on the Stokes components I (total intensity), Q (linear horizontal/vertical), and U (linear $\pm 45^\circ$). The acceptance function H_ρ is the same in each channel; what differs is that polarisation-sensitive photoreceptors weight Q and U by $\cos(2\theta_{\text{pref}})$ and $\sin(2\theta_{\text{pref}})$ of their preferred microvillar axis^{52,53}. The output is three sets of moiré spectra; the alias content carries polarisation information that the brain can read out.

The expected impact on the moiré mechanism specifically is modest. Moiré is fundamentally a high-contrast spatial-pattern phenomenon, which is a luminance effect (I channel). Polarisation mostly modifies long-range attraction^{8,10} — whether the biting diptera approaches the host at all, at distances beyond ~ 10 m where individual stripes are below the sampling resolution of the eye — whereas moiré modifies close-range fixation ($d \in [1, 2.5]$ m, the band identified in §4.2). The two mechanisms are largely orthogonal in the host-finding sequence; the present paper offers the moiré mechanism as complementary to,

not a replacement for, the polarotactic mechanism. Adding polarisation to the moiré pipeline is expected to refine the magnitude predictions but probably not change the conclusion.

4.6 Landing failure on striped hosts

Taken together, the matched-pair test of §4.2, the regional acute-zone analysis of §4.3 and the per-channel chromatic analysis of §4.4 converge on a single robust statement: the interaction of a striped zebra coat with the ommatidial sampling lattice of a high-resolution diurnal culicid compound eye necessarily generates a parasitic moiré signal whose magnitude is of order $\sim 8\%$ of the in-band brain-accessible signal in the close-approach band $d \in [1, 2.5]$ m. This figure is stable across receptor non-linearity (linear vs. Naka–Rushton), across eye region (acute zone, standard, periphery), across chromatic channel (R, G, B), and across a set of ($n = 28$) matched photographic pairs ($n = 28$). In every case the moiré signal disappears when the stripes alone are removed from the host while every other property of the scene is preserved, which establishes the stripe pattern as the proximate cause.

The optical-stage results above establish that a measurable parasitic spectrum survives into the brain-accessible passband; they say nothing yet about whether the fly’s downstream motion pathway is degraded by it. To close that gap we propagate one representative approach trajectory through the minimal Hassenstein–Reichardt elementary motion detector of §3.7 and report the resulting motion-energy time series in Fig. 9.

Figure 9 plots three motion-energy time series for the same approach trajectory. The grey curve $E_{\text{HR}}^{\text{clean}}(t)$ is the motion energy at the (Elementary Motion Detector) output when the comb-replication step (Eq. 9) is explicitly nulled: it is what an idealised diptera would see if its ommatidial lattice could sample without aliasing the stripe pattern. The black curve $E_{\text{HR}}^{\text{full}}(t)$ is the same quantity for the full ommatidial pipeline that does contain the aliased moiré of §2.7. The red curve is the signed difference $E_{\text{HR}}^{\text{moiré}}(t) = E_{\text{HR}}^{\text{full}}(t) - E_{\text{HR}}^{\text{clean}}(t)$ of Eq. 26, with the red shading indicating its sign relative to zero. The bottom axis is approach time at the photoreceptor frame interval $\Delta t = 30$ ms matched to the membrane time constant⁴⁵, and the top axis is the corresponding approach distance $d(t)$; the high-frequency ripple visible at $t \gtrsim 2.5$ s is the per-frame discrete crossing of stripes from one ommatidium to the next as the body grows in the field of view.

Two features of the curves are the central empirical result. First, both the clean and the full motion-energy traces rise monotonically as the host enters the close-approach band, but the alias-free trace rises faster: at the end of the trajectory ($d \approx 0.4$ m) the clean signal exceeds the full signal by a factor of ~ 2 . Second, $E_{\text{HR}}^{\text{moiré}}(t)$ is therefore strictly negative inside the close-approach band $d \in [1, 2.5]$ m and grows progressively more negative as the host seeking diptera closes in. The sign is the opposite of what would be expected if the moiré merely added a spurious motion signal of arbitrary direction: instead, the moiré is systematically cancelling coherent motion energy that the EMD array would otherwise produce. A direct algebraic decomposition of $E_{\text{HR}}^{\text{moiré}}$ into

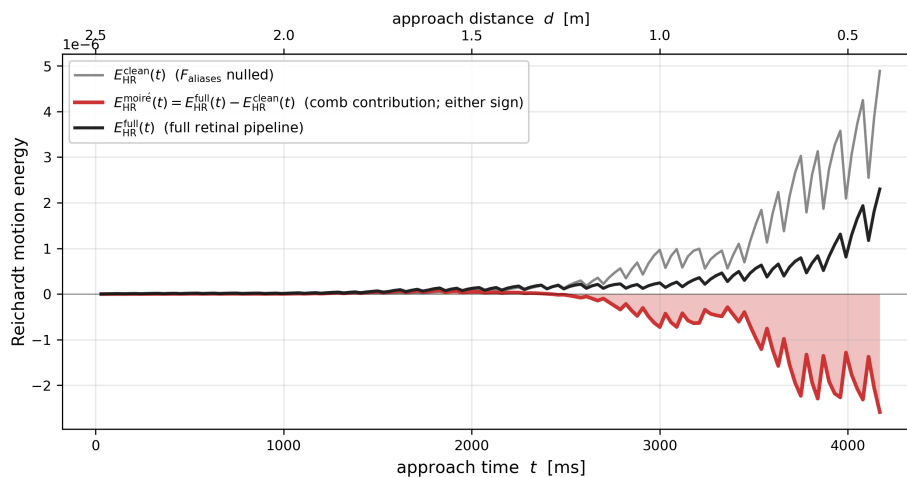


Figure 9: Reichardt motion-energy control on a striped host during a simulated close approach (DSC.0067, *Equus quagga*; $d_0 = 2.5$ m, $v_{\text{app}} = 0.5$ m s $^{-1}$, frame interval $\Delta t = 30$ ms). Grey: alias-free EMD output $E_{\text{HR}}^{\text{clean}}(t)$. Black: full ommatidial EMD output $E_{\text{HR}}^{\text{full}}(t)$. Red: their signed difference $E_{\text{HR}}^{\text{moiré}}(t)$ (Eq. 26). The moiré contribution is *negative* inside the close-approach band: aliased drift cancels the genuine motion percept at the EMD output rather than augmenting it. The cancellation is decomposed exactly in §S.5.

a cross-term and a self-term, reported in §S.5, attributes the negative sign to a destructive cross-correlation between the moiré component and the genuine-motion component of the signed EMD output, and shows independently that at 30% to 45% of ommatidia per frame the full pipeline’s local motion estimate carries the opposite direction to the alias-free pipeline’s. Aliased moiré drift contributes motion signal in directions inconsistent with the genuine self-motion translation, and the opponent subtraction of Eq. 24 cancels part of the genuine signal before squaring.

The behavioural reading is that the parasitic spectrum identified at the optical stage is not benign noise that the downstream brain could integrate out: it is a destructive contribution to the very motion-energy estimate that controls approach and landing in dipterans^{18–20}. An attacking dipteran approaching a striped host therefore loses, rather than gains, coherent expansion signal in exactly the close-approach window $d \in [1, 2.5]$ m that the optical-stage matched-pair test of §4.2 independently identifies as the moiré-peak band. A motion-energy deficit in this window is a documented cause of stalled landings in flies^{19,20}, and the same band coincides with the empirical terminal-hesitation phase^{5,7} in which biting Diptera approach a striped host but fail to settle. The optical-mechanism story is therefore not merely that stripes inject extra signal into the eye, but that the comb-step geometry of the ommatidial mosaic converts that injected signal, at the very next processing stage, into a partial

cancellation of the optic-flow estimate the biting diptera needs in order to land.

5 Conclusion

The reconstructed parasitic signal $I_{\text{par}}(x, y)$ and the resulting spurious motion energy provide a candidate optical mechanism for the failure of biting Diptera to land on striped hosts that has been documented in field studies^{5–9}. This mechanism is not contradictory to the polarotactic explanation of Horváth et al.¹⁰ and Egri et al.⁸: depolarisation of the white stripes disrupts long-range attraction, whereas moiré interference disrupts short-range fixation and landing. The two effects act at non-overlapping phases of the host-finding cascade and may have evolved in concert.

A Fourier model of diptera compound-eye sampling was developed and applied to images of zebra coats observed at biologically relevant viewing distances. A striped stimulus and a quasi-periodic sampling lattice, the optical interaction produces parasitic spatial frequencies that are not present in the stimulus itself; this follows directly from the convolution theorem and from the sampling theorem of Snyder¹³. When the model is parameterised with the published optical constants of diurnal Culicidae and Tabanidae^{15–17,54}, these parasitic frequencies fall within the spatial-frequency window in which host fixation and landing are controlled^{18–20}. The parasitic retinal signal is fed into a Hassenstein–Reichardt elementary motion detector^{44,45} and produces non-zero motion energy in directions that bear no relation to the true ego-motion of the diptera — an explanation for the landing failures and aborted touchdowns that have been documented in the field^{6,7,9}.

Several limitations should be made explicit. The presented optical Fourier model ignores higher-order neural processing in the lamina, medulla and lobula plate¹⁸ and the multimodal interactions with CO₂ and other olfactory cues that gate visual attraction in the first place^{32–34}. The presence of parasitic spatial frequencies at the retinal level nevertheless constitutes an unavoidable sensory perturbation under any plausible downstream architecture, and the Reichardt stage shows that this perturbation propagates into the motion stream that controls the final landing manoeuvre. The model thereby contributes an optics argument to the biting-fly hypothesis of zebra striping^{3,5,9} that is independent of the polarotaxis and silhouette-disruption mechanisms previously proposed^{8,10,11}.

Acknowledgements

The author thanks Tim Caro for providing the zebra images used for the analysis in this article. No external funding was received for this work. The simulation code is available from the author on reasonable request.

Supplementary Information

S.1 Gaussian approximation of the ommatidial acceptance

The compound-eye literature the angular acceptance function of a single ommatidium can be approximated by a two-dimensional Gaussian. Under this approximation the low-pass envelope of (Eq. 5) becomes

$$H_\rho^G(u, v) = \exp\left(-\frac{u^2 + v^2}{2\sigma_f^2}\right), \quad \sigma_f = \frac{1}{2\pi\sigma_\rho}, \quad (27)$$

where σ_ρ is the half-width at half-maximum of the acceptance angle expressed in degrees. For diurnal culicids ($\Delta\varphi \approx 2^\circ$ ^{15,16}) the canonical choice is $\sigma_\rho = 0.85^\circ$. The Gaussian form is analytically convenient and captures the central lobe of (Eq. 6) reasonably well, but it lacks a hard cutoff and underestimates attenuation near ρ_c ; we therefore retain the Airy-based expression (Eq. 7) in the main analysis and include (Eq. 27) here for comparison.

S.2 FFT-pipeline numerical controls

Two numerical controls are applied on every distance to report relative error.

(i) Round-trip control on F_{blurred} . The complex spectrum $F_{\text{blurred}} = \mathcal{F}\{I_{\text{blurred}} w\}$ carries both amplitude and phase. Inverse-transforming it must recover the windowed blurred image up to floating-point precision,

$$\|\text{Re } \mathcal{F}^{-1}\{F_{\text{blurred}}\} - I_{\text{blurred}} \cdot w\|_\infty / \|I_{\text{blurred}} \cdot w\|_\infty \lesssim 10^{-15}. \quad (28)$$

(ii) Round-trip control on F_{repl} . By Eq. 9 and the convolution theorem, $\mathcal{F}^{-1}\{F_{\text{repl}}\}$ must equal $I_{\text{blurred}} \cdot w$ multiplied by the spatial Dirichlet approximation of the comb $\text{III}_{\Delta\varphi}$ used in the construction. The result is real to within $|\text{Im } \mathcal{F}^{-1}\{F_{\text{repl}}\}|_\infty \lesssim 10^{-15}$, the floating-point noise level. A non-zero imaginary part above this threshold would indicate a misordered `fftshift/ifftshift` or an asymmetric replica sum.

A third, indirect Wiener–Khinchin check $\mathcal{F}^{-1}\{|F_{\text{blurred}}|^2\}|_{(0,0)} = \sum_{x,y} |I_{\text{blurred}}(x,y) w(x,y)|^2$ (Parseval’s theorem) holds to relative error $\lesssim 10^{-16}$, within a single floating-point ULP. The three checks together verify the FFT pipeline at every stage of Eqs. 9–15.

S.3 Photoreceptor non-linearity

The Naka–Rushton form (Eq. 12) is one option for the photoreceptor non-linearity; the framework also supports a second, complementary, form: a truncated *Volterra* polynomial expanded around the local mean intensity^{48,55}. For

an input image I of mean μ and standard deviation σ , the Volterra non-linearity is

$$\text{Volt}_{a_2, a_3}(I(x, y)) = \mu + (I - \mu) + a_2(I - \mu)^2 + a_3(I - \mu)^3, \quad (29)$$

followed by a passive rescaling that preserves μ and σ so that a_2, a_3 parameterise the shape of the non-linearity rather than its overall gain or DC offset (which would be absorbed by downstream normalisation anyway). The quadratic kernel a_2 generates harmonics at $2f$ and intermodulation products $f_1 \pm f_2$ between any two stimulus frequencies; the cubic kernel a_3 generates $3f$ and $2f_1 \pm f_2$. Both kernels are folded into $F_{\text{blurred}}^{\text{NL}}$ and propagate through the comb / H_{box} stages in exactly the same way as the linear content, so Eq. 14 applies unchanged.

The two forms are not in competition: Naka–Rushton is a saturating function whose local Taylor expansion around the operating point yields negative quadratic and cubic Volterra coefficients; the Volterra form makes those coefficients independently tunable, which is what makes it useful for sensitivity analyses. Empirically the two forms agree on the location of the moiré peak and on its magnitude to within $\sim 2\%$ at the peak distance; off-peak they differ more visibly because Naka–Rushton’s compression preferentially attenuates bright stripes whereas Volterra’s polynomial creates weak intermodulation in the alias-generating band (see §4 for the empirical comparison and quantitative numbers). Naka–Rushton is adopted as non-linearity throughout the analysis of this paper because it is the more biologically motivated of the two forms; the Volterra option is retained as a generic check on the harmonic and intermodulation structure that any analytic photoreceptor non-linearity must generate.

S.4 Body-height calibration

The simulation pipeline of §3 converts the body’s pixel count $h_{\text{body, pix}}$ into the camera distance d_{cam} through Eq. 20, using a generic body height $h_{\text{body}} = 1.4\text{ m}$ for *Equus quagga*. The simulated approach trajectory is then generated by isotropic crop scaling around the body centre: at each simulated distance d the script extracts a crop of side (d/d_{cam}) FoV/dpp_{cam} camera pixels (§3.1). The combined effect is that the true body height h_{true} enters the model only through the angular projection h_{true}/d , and $(h_{\text{true}}, d_{\text{true}})$ and (h_{body}, d) are angularly indistinguishable whenever $h_{\text{true}}/d_{\text{true}} = h_{\text{body}}/d$.

This scale invariance fully determines the propagation of the calibration error. If the true body height differs from the generic value, the retinal image labelled “ d ” by the simulation corresponds to the real-world distance

$$d_{\text{true}} = d \cdot \frac{h_{\text{true}}}{h_{\text{body}}}, \quad (30)$$

so the entire $E_{\text{par, rel}}(d)$ curve translates on the d -axis by the multiplicative factor $h_{\text{true}}/h_{\text{body}}$. The peak position inherits exactly this shift, $\Delta d_{\text{peak}}/d_{\text{peak}} = \Delta h/h_{\text{body}}$, while the peak amplitude is left invariant — the curve shape is

preserved under the rescaling because every retinal spatial-frequency content at the new “ d_{true} ” is identical to that at the old “ d ” by construction.

For an inter-individual range $1.35 \text{ m} \leq h_{\text{true}} \leq 1.45 \text{ m}$ around $h_{\text{body}} = 1.4 \text{ m}$ (*Equus quagga* shoulder height³), the relative uncertainty is $\pm 3.57\%$. Applied to the empirical peak at $d_{\text{peak}} \approx 1.6 \text{ m}$ (§4.2) this gives

$$\Delta d_{\text{peak}} = d_{\text{peak}} \cdot \frac{\Delta h}{h_{\text{body}}} = 1.6 \text{ m} \cdot \frac{\pm 0.05 \text{ m}}{1.4 \text{ m}} \approx \pm 5.7 \text{ cm}, \quad (31)$$

so the moiré peak lies in the range $d_{\text{peak}} \in [1.54 \text{ m}, 1.66 \text{ m}]$ when the per-individual height is varied across its observed range. This uncertainty is one order of magnitude smaller than the natural width of the peak (the close-approach band $d \in [1, 2.5] \text{ m}$ identified in §?? has a half-width of order 0.75 m), so the substantive claim of §4.6 — that the moiré mechanism peaks inside the documented terminal-hesitation window — is unaffected by the calibration uncertainty. The peak amplitude $\sim 8\%$ reported in §4.2 is unaffected by construction.

For matched-pair comparisons within the dataset, the same scaling applies independently to each pair: per-individual height variation shifts the per-pair peak distance by at most $\pm 6 \text{ cm}$ relative to the cohort mean, which sets the floor for the horizontal scatter visible in the thin per-pair traces of Fig. 6.

S.5 Diagnostic for the Reichardt motion-energy control

The matched full / clean Reichardt control of §4.6 reports a strictly negative moiré contribution $E_{\text{HR}}^{\text{moiré}}(t) = E_{\text{HR}}^{\text{full}}(t) - E_{\text{HR}}^{\text{clean}}(t)$ (Eq. 26) inside the close-approach band. Because E_{HR} is the difference of two mean-squared signed EMD outputs — not the squared magnitude of a difference — the negative sign admits two mutually exclusive mechanistic readings, and only one of them is consistent with a moiré-induced cancellation of the genuine motion percept. To distinguish them $E_{\text{HR}}^{\text{moiré}}(t)$ is decomposed exactly.

Write the full-pipeline EMD output as $\text{HR}^{\text{full}}(t) = \text{HR}^{\text{clean}}(t) + \Delta \text{HR}(t)$, where $\Delta \text{HR}(t) = \text{HR}^{\text{full}}(t) - \text{HR}^{\text{clean}}(t)$ is the moiré-induced additive contribution to the signed EMD output. Squaring and averaging across the detector array gives the algebraic identity

$$E_{\text{HR}}^{\text{moiré}}(t) = \underbrace{2 \langle \text{HR}^{\text{clean}}(t) \Delta \text{HR}(t) \rangle}_{\text{CROSS}(t)} + \underbrace{\langle \Delta \text{HR}(t)^2 \rangle}_{\text{SELF}(t)}, \quad (32)$$

where $\langle \cdot \rangle$ denotes the spatial average over the ommatidial array, summed over the horizontal and vertical EMD components. $\text{SELF}(t)$ is the motion energy that the moiré contribution would carry on its own and is non-negative by construction. $\text{CROSS}(t)$ is twice the inner product of the moiré-only EMD signal with the genuine-motion EMD signal and is signed: positive if the two are spatially co-oriented (constructive interference, moiré drift aligned with the genuine optic flow) and negative if they are anti-oriented (destructive interference, moiré drift opposed to the genuine optic flow). Eq. 32 is algebraically exact and is

verified numerically frame-by-frame to a residual $\lesssim 10^{-20}$ (single ULP of the floating-point sum), so any departure of the moiré curve from CROSS + SELF in Fig. 10 is a code-side bug, not an interpretation.

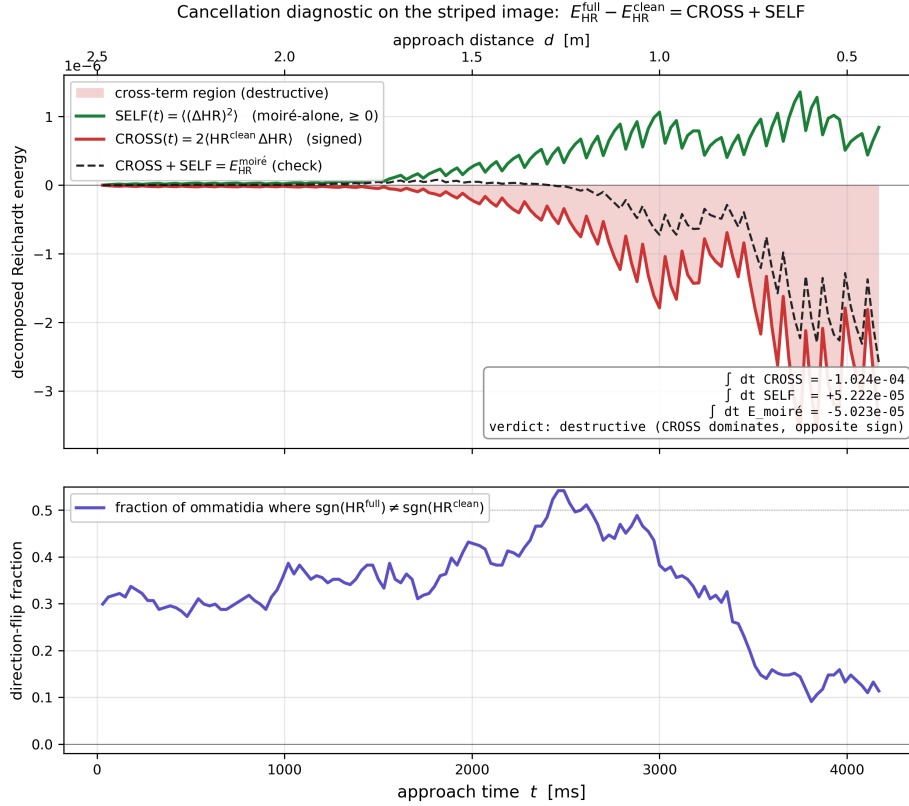


Figure 10: Per-frame decomposition of the moiré contribution to the Reichardt motion energy, $E_{HR}^{\text{moiré}}(t) = \text{CROSS}(t) + \text{SELF}(t)$ (Eq. 32), on the approach trajectory of Fig. 9. **Top:** SELF(t) (green; moiré-alone motion energy, non-negative), CROSS(t) (red; signed inner product of the moiré and clean EMD outputs), and their sum (dashed; equal to $E_{HR}^{\text{moiré}}$ to machine precision). The annotation reports the time integrals and the qualitative verdict. **Bottom:** fraction of ommatidia per frame at which the full pipeline’s EMD output carries the opposite sign to the alias-free pipeline’s, i.e. the fraction of local motion detectors whose direction is flipped by the comb step.

Figure 10 reports the decomposition for the representative approach trajectory of Fig. 9. The top panel shows three curves. SELF(t) is positive and small. CROSS(t) is negative throughout the close-approach band and dominates SELF(t) in magnitude by a factor of ~ 2 . Their sum reproduces the moiré curve of Fig. 9 (dashed black). The time integrals printed in the corner box

make the magnitude ordering explicit: $|\int \text{CROSS}(t) dt|$ exceeds $\int \text{SELF}(t) dt$, so the integrated $E_{\text{HR}}^{\text{moiré}}$ inherits the negative sign of $\text{CROSS}(t)$. This is the decisive observation: the moiré contribution to the EMD output is dominated by its cross- term with the genuine-motion signal — the very term that vanishes for any moiré drift parallel to the genuine optic flow — and is therefore not simply additive noise. Aliased moiré drift is correlated with the clean EMD output in the orientation-opposed sense, which by definition is destructive interference at the signed-output level.

The bottom panel provides an independent confirmation that does not rely on the algebraic decomposition. At each frame the fraction of ommatidia at which the full and clean EMD outputs carry opposite signs is recorded: i.e. the fraction of local motion detectors that report leftward motion when the alias-free baseline reports rightward motion, or vice versa. If aliasing were producing purely same-direction motion blur this fraction would stay close to zero. If it were producing motion of random direction relative to the genuine signal the fraction would converge to 50%. The observed fraction is consistently in the 30% to 45% band across the entire close-approach window, dropping only when the host begins to fill the entire 30° simulated field of view at $d \lesssim 0.6\text{ m}$. A third of all local motion detectors flipping the direction of their EMD output because of the comb step is a strong qualitative confirmation that the moiré in this stimulus class is not predominantly co-oriented with the genuine self-motion: it carries the geometric signature of folded-band aliasing, where stripe content at spatial frequencies near and above the eye-Nyquist boundary aliases into low-frequency moiré patterns whose effective drift velocity has the opposite sign to the underlying stripe motion. Together with Eq. 32, this constitutes the quantitative basis for the destructive-interference reading of Fig. 9 adopted in §4.6.

References

- [1] Charles Darwin. *The Descent of Man, and Selection in Relation to Sex*, volume 2. John Murray, London, 1871.
- [2] Alfred Russel Wallace. Mimicry, and other protective resemblances among animals. *Westminster Foreign Quarterly Review*, 31:1–43, 1867.
- [3] Tim Caro, Amanda Izzo, Robert C. Reiner, Hannah Walker, and Theodore Stankowich. The function of zebra stripes. *Nature Communications*, 5:3535, 2014. doi: 10.1038/ncomms4535.
- [4] Brenda Larison, Ryan J. Harrigan, Henri A. Thomassen, Daniel I. Rubenstein, Alec M. Chan-Golston, Elizabeth Li, and Thomas B. Smith. How the zebra got its stripes: a problem with too many solutions. *Royal Society Open Science*, 2:140452, 2015. doi: 10.1098/rsos.140452.
- [5] Jeffrey K. Waage. How the zebra got its stripes: biting flies as selective

- [16] Michael F. Land, Gabriella Gibson, Joanna Horwood, and Jochen Zeil. Fundamental differences in the optical structure of the eyes of nocturnal and diurnal mosquitoes. *Journal of Comparative Physiology A*, 185:91–103, 1999. doi: 10.1007/s003590050369.
- [17] H. Kawada, H. Tatsuta, K. Arikawa, and M. Takagi. Comparative study on the relationship between photoperiodic host-seeking behavioral patterns and the eye parameters of mosquitoes. *Journal of Insect Physiology*, 52: 67–75, 2006.
- [18] Alexander Borst. Fly visual course control: behaviour, algorithms, and circuits. *Nature Reviews Neuroscience*, 15:590–599, 2014.
- [19] Floris van Breugel and Michael H. Dickinson. The visual control of landing and obstacle avoidance in the fruit fly *drosophila melanogaster*. *Journal of Experimental Biology*, 215:1783–1798, 2012. doi: 10.1242/jeb.066498.
- [20] Emily Baird, Norbert Boeddeker, Michael R. Ibbotson, and Mandyam V. Srinivasan. A universal strategy for visually guided landing. *Proceedings of the National Academy of Sciences USA*, 110:18686–18691, 2013.
- [21] Rudyard Kipling. *Just So Stories*. Macmillan, London, 1908.
- [22] Gerald H. Thayer. *Concealing-coloration in the animal kingdom*. Macmillan, London, 1909.
- [23] Hugh B. Cott. *Adaptive Coloration in Animals*. Methuen, London, 1940.
- [24] Graeme D. Ruxton. The possible fitness benefits of striped coat coloration for zebra. *Mammal Review*, 32(4):237–244, 2002. doi: 10.1046/j.1365-2907.2002.00108.x.
- [25] Tim Caro. Contrasting coloration in terrestrial mammals. *Philosophical Transactions of the Royal Society B*, 364:537–548, 2009.
- [26] M. Stevens, D. H. Yule, and Graeme D. Ruxton. Dazzle coloration and prey movement. *Proceedings of the Royal Society B*, 275:2639–2643, 2008.
- [27] M. Stevens, W. T. L. Searle, J. E. Seymour, K. L. A. Marshall, and Graeme D. Ruxton. Motion dazzle and camouflage as distinct anti-predator defences. *BMC Biology*, 9:81, 2011.
- [28] Nicholas E. Scott-Samuel, Roland Baddeley, Chloe E. Palmer, and Innes C. Cuthill. Dazzle camouflage affects speed perception. *PLoS ONE*, 6(6): e20233, 2011. doi: 10.1371/journal.pone.0020233.
- [29] Alison Cobb and Stephen Cobb. Do zebra stripes influence thermoregulation? *Journal of Natural History*, 53:863–879, 2019. doi: 10.1080/00222933.2019.1607600.

- [30] Gábor Horváth, Ádám Pereszlényi, Dénes Száz, András Barta, Imre M. Jánosi, Balázs Gerics, and Susanne Åkesson. Experimental evidence that stripes do not cool zebras. *Scientific Reports*, 8:9351, 2018. doi: 10.1038/s41598-018-27637-1.
- [31] Miklós Blahó, Ádám Egri, Dénes Száz, György Kriska, Susanne Åkesson, and Gábor Horváth. Stripes disrupt odour attractiveness to biting horseflies: battle between ammonia, CO₂, and colour pattern for dominance in the sensory systems of host-seeking tabanids. *Physiology and Behavior*, 119:168–174, 2013. doi: 10.1016/j.physbeh.2013.06.013.
- [32] Iliano V. Coutinho-Abreu, Jeffrey A. Riffell, and Omar S. Akbari. Human attractive cues and mosquito host-seeking behavior. *Trends in Parasitology*, 38(3):253–264, 2022.
- [33] Conor J. McMeniman, Roman A. Corfas, Benjamin J. Matthews, Scott A. Ritchie, and Leslie B. Vosshall. Multimodal integration of carbon dioxide and other sensory cues drives mosquito attraction to humans. *Cell*, 156:1060–1071, 2014.
- [34] Floris Van Breugel, Jeffrey Riffell, Adrienne Fairhall, and Michael H. Dickinson. Mosquitoes use vision to associate odor plumes with thermal targets. *Current Biology*, 25:2123–2129, 2015.
- [35] F. M. Hawkes, J. Zeil, and G. Gibson. Vision in mosquitoes. In R. Ignell, C. R. Lazzari, M. G. Lorenzo, and S. R. Hill, editors, *Sensory Ecology of Disease Vectors*, pages 509–534. Wageningen Academic Publishers, 2022. doi: 10.3920/978-90-8686-932-9_19.
- [36] Eric J. Warrant. Seeing better at night: life style, eye design and the optimum strategy of spatial and temporal summation. *Vision Research*, 39:1611–1630, 1999.
- [37] Joseph W. Goodman. *Introduction to Fourier Optics*. Roberts & Company Publishers, Englewood, CO, 3 edition, 2005. ISBN 978-0-9747077-2-3.
- [38] Max Born and Emil Wolf. *Principles of Optics: Electromagnetic Theory of Propagation, Interference and Diffraction of Light*. Cambridge University Press, Cambridge, 7 edition, 1999. ISBN 978-0-521-64222-4.
- [39] K. Kirschfeld. Die Projektion der optischen Umwelt auf das Raster der Rhabdomere im Komplexauge von *Musca*. *Experimental Brain Research*, 3:248–270, 1967. doi: 10.1007/BF00235588.
- [40] S. B. Laughlin. A simple coding procedure enhances a neuron’s information capacity. *Zeitschrift für Naturforschung C*, 36(9–10):910–912, 1981. doi: 10.1515/znc-1981-9-1040.

- [41] Molly Z. Liu and Leslie B. Vosshall. General visual and contingent thermal cues interact to elicit attraction in female *aedes aegypti* mosquitoes. *Current Biology*, 29:2250–2257, 2019.
- [42] Dan-Eric Nilsson. Optics and evolution of the compound eye. pages 30–73, 1989.
- [43] Hitoshi Kawada, Shin-ya Takemura, Kentaro Arikawa, and Masahiro Takagi. Comparative study on nocturnal behavior of *Aedes aegypti* and *Aedes albopictus*. *Journal of Medical Entomology*, 42(3):312–318, 2005.
- [44] Bernhard Hassenstein and Werner Reichardt. Systemtheoretische Analyse der Zeit-, Reihenfolgen- und Vorzeichenauswertung bei der Bewegungsperzeption des Rüsselkäfers *chlorophanus*. *Zeitschrift für Naturforschung B*, 11:513–524, 1956.
- [45] Alexander Borst, Jürgen Haag, and Dierk F. Reiff. Fly motion vision. *Annual Review of Neuroscience*, 33:49–70, 2010.
- [46] Simon B. Laughlin. The role of sensory adaptation in the retina. *Journal of Experimental Biology*, 146:39–62, 1989. doi: 10.1242/jeb.146.1.39.
- [47] Jonathan Howard, Andreas Dubs, and Roger Payne. The dynamics of phototransduction in insects. *Journal of Comparative Physiology A*, 154(5):707–718, 1984. doi: 10.1007/BF01350224.
- [48] J. H. van Hateren. A theory of maximizing sensory information. *Biological Cybernetics*, 68(1):23–29, 1992. doi: 10.1007/BF00203134.
- [49] Xiaobang Hu, M. A. Whaley, M. M. Stein, B. E. Mitchell, and J. E. O’Tousa. Coexpression of spectrally distinct rhodopsins in *aedes aegypti* R7 photoreceptors. *PLOS ONE*, 9(1):e85780, 2014. doi: 10.1371/journal.pone.0085780.
- [50] Yinpeng Zhan, Diego Alonso San Alberto, Claire Rusch, Jeffrey A. Riffell, and Craig Montell. Elimination of vision-guided target attraction in *aedes aegypti* using CRISPR. *Current Biology*, 31(18):4180–4187, 2021. doi: 10.1016/j.cub.2021.07.003.
- [51] Almut Kelber, Misha Vorobyev, and Daniel Osorio. Animal colour vision – behavioural tests and physiological concepts. *Biological Reviews*, 78(1): 81–118, 2003. doi: 10.1017/S1464793102006020.
- [52] Matt Wachowiak and Lawrence B. Cohen. Polarization sensitivity in the *aedes aegypti* eye. *Journal of Comparative Physiology A*, 177:325–332, 1995. doi: 10.1007/BF00192421.
- [53] Thomas Labhart and Erich P. Meyer. Detectors for polarized skylight in insects: A survey of ommatidial specializations in the dorsal rim area of the compound eye. *Microscopy Research and Technique*, 47(6):368–379,

1999. doi: 10.1002/(SICI)1097-0029(19991215)47:6<368::AID-JEMT2>3.0.CO;2-Q.

- [54] Roger C. Hardie, K. Vogt, and A. Rudolph. The compound eye of the tsetse fly (*glossina morsitans morsitans* and *glossina palpalis palpalis*). *Journal of Insect Physiology*, 35:423–431, 1989.
- [55] Vito Volterra. *Theory of Functionals and of Integral and Integro-Differential Equations*. Blackie & Son, London, 1930.